JGR Planets

RESEARCH ARTICLE

10.1029/2025JE009463

Intrusion-Induced Forced Folding Model for the Origin of Séítah Formation Domes on the Jezero Crater Floor, Mars

Robert Barnes[1], Sanjeev Gupta[1], Allan Treiman[2], Steven Sholes[3], Gerhard Paar[4], Christian Tate[5], Andreas Bechtold[6,7], Katie Stack-Morgan[3], James F. Bell III[8], Justin Maki[3], Briony Horgan[9], Jorge Nuñez[10], Chris Traxler[11], Thomas Ortner[4,11], Emileigh S. Shoemaker Thackston[12,13,14], Svein-Erik Hamran[15], Sanna Alwmark[16], Melissa Rice[17], Vivian Sun[3], Olivier Beyssac[18], Andrew Annex[19], Adrian Brown[20], Linda Kah[21], David Flannery[22], Justin I. Simon[23], Sebastian Walter[24], Keyron Hickman-Lewis[25], and Ken Farley[3]

[1]Department of Earth Science & Engineering, Imperial College London, London, UK, [2]Lunar and Planetary Institute (USRA), Houston, TX, USA, [3]Jet Propulsion Laboratory, California Institute of Technology, Pasadena, CA, USA, [4]Joanneum Research Institute for Digital Technologies, Graz, Austria, [5]Malin Space Science Systems, San Diego, CA, USA, [6]Department of Lithospheric Research, University of Vienna, Vienna, Austria, [7]Austrian Academy of Sciences, Vienna, Austria, [8]School of Earth and Space Exploration, Arizona State University, Tempe, AZ, USA, [9]Department of Earth, Atmospheric, and Planetary Sciences, Purdue University, West Lafayette, IN, USA, [10]Johns Hopkins University Applied Physics Laboratory, Laurel, MD, USA, [11]VRVis GmbH, Vienna, Austria, [12]Department of Astronomy, University of Maryland, College Park, MD, USA, [13]JPL Goddard Space Flight Center, Greenbelt, MD, USA, [14]Center for Research and Exploration in Space Science and Technology, JPL/GSFC, Greenbelt, MD, USA, [15]Center for Space Sensors and Systems, University of Oslo, Oslo, Norway, [16]Department of Earth and Environmental Sciences, Lund University, Lund, Sweden, [17]Geology Department, Western Washington University, Bellingham, WA, USA, [18]Institut de Minéralogie, de Physique des Matériaux et de Cosmochimie, CNRS UMR 7590, Sorbonne Université, Muséum National d'Histoire Naturelle, Paris, France, [19]Carl Sagan Center, SETI Institute, Mountain View, CA, USA, [20]Plancius Research, Manlius, NY, USA, [21]Department of Earth and Planetary Sciences, University of Tennessee, Knoxville, TN, USA, [22]School of Earth and Atmospheric Sciences, Queensland University of Technology, Brisbane, QLD, Australia, [23]Astromaterials Research and Exploration Science Division, JPL Johnson Space Center, Houston, TX, USA, [24]Institute of Geological Sciences, Planetary Sciences and Remote Sensing Group, Freie Universität Berlin, Berlin, Germany, [25]School of Natural Sciences, Birkbeck, University of London, London, UK

Key Points:

- The Séítah and Máaz formations were emplaced and later folded into a broad, flat-crested dome with dipping limbs
- Folding is best explained by intrusion-driven uplift from an underlying sill or laccolith, rather than regional tectonic or impact processes
- Structural uplift raised Séítah outcrops topographically above Máaz outcrops, explaining why the cumulates sit higher than younger lava

Supporting Information:

Supporting Information may be found in the online version of this article.

Correspondence to:

R. Barnes and S. Gupta,
robert.barnes@imperial.ac.uk;
s.gupta@imperial.ac.uk

Citation:

Barnes, R., Gupta, S., Treiman, A., Sholes, S., Paar, G., Tate, C., et al. (2026). Intrusion-induced forced folding model for the origin of Séítah formation domes on the Jezero crater floor, Mars. *Journal of Geophysical Research: Planets*, *131*, e2025JE009463. https://doi.org/10.1029/2025JE009463

Received 3 OCT 2025
Accepted 28 FEB 2026

Author Contributions:

Conceptualization: Robert Barnes, Sanjeev Gupta, Allan Treiman, Ken Farley
Data curation: Gerhard Paar, James F. Bell III, Justin Maki, Thomas Ortner, Svein-Erik Hamran, Sanna Alwmark, Vivian Sun, Andrew Annex, Sebastian Walter
Formal analysis: Robert Barnes, Sanjeev Gupta, Allan Treiman, Steven Sholes, Christian Tate, Briony Horgan, Jorge Nuñez, Emileigh S. Shoemaker Thackston, Sanna Alwmark, Melissa Rice, Olivier Beyssac, Justin I. Simon, Ken Farley

Abstract

The JPL rover Perseverance's investigations of Jezero crater's floor reveal that the ultramafic Séítah formation and the overlying mafic Máaz formation are deformed into a broad, low-amplitude structural dome. Mastcam-Z stereo images processed into digital outcrop models, together with RIMFAX ground-penetrating radar profiles, were used to reconstruct the three-dimensional stratal geometry of both units along a SW–NE transect across a southern domain of the dome called south Séítah. Measurements from 3-D reconstructions show a progression from sub-horizontal layers in the central parts of the dome to dips <20° away from the dome on its flanks, with Máaz and underlying Séítah layers dipping concordantly. RIMFAX profiles and imaging around the dome confirm that limb dips are continuous into the subsurface and form a flat-crested composite quaquaversal fold structure. Séítah rocks in the fold core are up to 17 m higher than adjacent Máaz lava flows, despite stratigraphically underlying them, a relationship attributed to structural uplift. Fold geometry, wavelength (~1 km), and amplitude (~30–50 m), match models of forced folding produced by inflation of shallow igneous intrusions. The most likely cause is the emplacement of a sill or laccolith beneath the crater floor, generating elastic bending of the overlying layers. This intrusion-driven uplift explains Séítah's elevated position, constrains the deformation history of Jezero's crater floor units post-emplacement of the Séítah and Máaz formations, and supports a significant role for shallow magmatic intrusion in shaping intracrustal structures on Mars.

Plain Language Summary

The *Perseverance* rover has revealed that igneous rocks on Jezero crater's floor are not flat lying, but gently folded into a broad dome. The lower unit, the Séítah formation, is made of olivine-rich intrusive igneous rocks, and appears topographically above the overlying Máaz formation basaltic lava. Using rover stereo images, ground-penetrating radar, and orbital topography, we have reconstructed the three-dimensional structure of these rocks. Both formations tilt away from the dome's center, forming a fold about 1 km wide and tens of meters high. The best explanation is that magma intruded beneath the crater floor after Séítah and Máaz rocks formed. As the magma pooled in a sill or laccolith, it pushed the

Funding acquisition: Sanjeev Gupta, Gerhard Paar, Katie Stack-Morgan, James F. Bell III, Justin Maki, Chris Traxler
Investigation: Robert Barnes, Sanjeev Gupta, Allan Treiman, Steven Sholes, Christian Tate, Andreas Bechtold, Katie Stack-Morgan, James F. Bell III, Justin Maki, Briony Horgan, Jorge Nuñez, Emileigh S. Shoemaker Thackston, Svein-Erik Hamran, Sanna Alwmark, Melissa Rice, Vivian Sun, Olivier Beyssac, Andrew Annex, Adrian Brown, Linda Kah, David Flannery, Justin I. Simon, Sebastian Walter, Keyron Hickman-Lewis, Ken Farley
Methodology: Robert Barnes, Sanjeev Gupta, Steven Sholes, Gerhard Paar, Christian Tate, Andreas Bechtold, James F. Bell III, Briony Horgan, Jorge Nuñez, Chris Traxler, Thomas Ortner, Svein-Erik Hamran, Melissa Rice, Vivian Sun, Olivier Beyssac
Project administration: Sanjeev Gupta, Katie Stack-Morgan, James F. Bell III, Justin Maki, Ken Farley
Resources: Justin Maki
Software: Gerhard Paar, Chris Traxler, Thomas Ortner
Supervision: Sanjeev Gupta, Katie Stack-Morgan, James F. Bell III
Validation: Gerhard Paar
Visualization: Robert Barnes, Gerhard Paar, Christian Tate, Andreas Bechtold, Justin Maki, Jorge Nuñez, Chris Traxler, Thomas Ortner, Svein-Erik Hamran, Melissa Rice, Sebastian Walter
Writing – original draft: Robert Barnes, Sanjeev Gupta, Allan Treiman, Steven Sholes, Gerhard Paar, Chris Traxler, Justin I. Simon
Writing – review & editing: Robert Barnes, Sanjeev Gupta, Allan Treiman, Gerhard Paar, Andreas Bechtold, Briony Horgan, Chris Traxler, Emileigh S. Shoemaker Thackston, Olivier Beyssac, Adrian Brown, Linda Kah, Justin I. Simon

overlying rocks upward, bending them into a dome. Similar "forced folds" are well known on Earth. This discovery shows that shallow intrusions shaped Mars' crust and provides key contextual information for igneous rock samples collected from the crater floor for return to Earth.

1. Introduction

The discovery of a suite of igneous rocks in Jezero crater by the Perseverance rover provides important insight into Martian magmatic processes. The rover landed on the western floor of Jezero crater in February 2021, and in her first year of exploration, she was dedicated to characterizing the geology of the crater floor and collecting samples for return to Earth (Bell et al., 2022; Crumpler et al., 2023; Farley et al., 2020; Simon et al., 2023). Prior to landing, geological mapping inside Jezero crater using orbital data showed two distinct units: a stratigraphically lower unit named the Crater Floor Fractured 1 (Cf-f-1) unit and an upper overlying crater-retaining unit named the Crater Floor Fractured Rough (Cf-fr) unit (Goudge et al., 2015; Stack et al., 2020; Sun & Stack, 2020). These units have distinct surface morphologies (see their names) and reflectance spectra, with Cf-fr interpreted to contain pyroxene and the Cf-f-1 unit interpreted to contain abundant olivine and some carbonate (Horgan et al., 2023).

Rover-based in situ investigations by *Perseverance* demonstrated that these two orbitally derived units correspond to two suites of igneous rocks: the Séítah formation (Cf-f-1) of ultramafic composition, and the mafic to intermediate Máaz formation (Cf-fr) (Beyssac et al., 2023; Farley et al., 2022; Hernández-Montenegro et al., 2025; Horgan et al., 2023; Liu et al., 2022; Treiman et al., 2025; Udry et al., 2023; Wiens et al., 2022;). The Séítah formation (where "Séítah" is Navajo for "amidst the sands") is interpreted as a coarsely crystalline olivine-bearing cumulate based on textural, mineralogical and geochemical evidence (Beyssac et al., 2023; Farley et al., 2022; Hernández-Montenegro et al., 2025; Liu et al., 2022; Treiman et al., 2025; Wiens et al., 2022;). The discovery of an olivine cumulate lithology in the Jezero crater floor was unexpected for the Mars 2020 mission. Possible interpretations for an emplacement mechanism for the Séítah formation include crystallization from a thick lava flow, a lava lake, impact melt sheet, or in a sill (Farley et al., 2022). The overlying Máaz formation (where "Máaz" is the Navajo name for Mars) is interpreted as a series of flows of highly evolved basalt, consisting principally of the minerals pyroxene and plagioclase (Alwmark et al., 2023; Bell et al., 2022; Crumpler et al., 2023; Hernandez-Montenegro et al., 2025; Horgan et al., 2023; Udry et al., 2023; Wiens et al., 2022).

Whilst the Máaz formation clearly overlies the Séítah formation physically, the structural and chemical relationships between the two formations are not clear. Two models have been proposed. In one model, the Séítah cumulate formed by crystal settling of the olivine crystals in a basaltic magma body such as a thick lava flow, lava lake, or sill (Beyssac et al., 2023; Farley et al., 2022; Liu et al., 2022). This then cooled and was eroded prior to the emplacement of the unrelated Máaz lava flows on an erosional surface on top of the Séítah rocks (Beyssac et al., 2023; Udry et al., 2023; Wiens et al., 2022). In the second model, the Séítah and Máaz rocks are considered to be related and derived from similar magma sources, with the Máaz basalts having crystallized from a magma melt complementary to the cumulate melt that formed Séítah (Treiman et al., 2025; Wiens et al., 2022). This model suggests a petrogenetic relationship between Séítah and Máaz (Hernández-Montenegro et al., 2025; Treiman et al., 2025).

Recent studies that have explored the geochemical association of the Séítah olivine cumulate with the Máaz basalts from petrological, mineralogical and modeling investigations support a link between the Máaz formation parent melt and the Séítah cumulate (Hernández-Montenegro et al., 2025; Treiman et al., 2025). However, the structural relation and timing of emplacement of the Séítah and Máaz rocks remain poorly constrained, limiting our understanding of the emplacement mechanisms of these two rock suites.

Here we examine the structural relationship between the Séítah and Máaz formations. Initial investigations indicated that (a) the Máaz formation physically overlies the Séítah formation, but the rocks of the Séítah formation are commonly topographically higher in elevation than adjacent Máaz formation rocks (Farley et al., 2022), and (b) that the Máaz and Séítah layers are tilted close to their contact (Farley et al., 2022; Hamran et al., 2022). Robust models for the emplacement processes of these two igneous units require these observations to be considered.

This study describes the structural geometry of the Séítah and Máaz formations in the south Séítah area of the Jezero crater floor explored by *Perseverance*. We determine rock layer dips and strikes from digital outcrop models derived from stereo images collected by the Mastcam-Z instrument onboard *Perseverance*. These data,

coupled with analysis of orbitally derived topographic data and subsurface radar data from the RIMFAX instrument, enable construction of a structural cross-section across part of the Séítah structure and lead to an interpretation that it represents a forced fold. We develop a model that proposes that forced folding is a consequence of intrusion-driven uplift likely by sill or laccolith emplacement in the subsurface. Our structural model provides geologic context for Perseverance's suite of igneous rock samples collected on the crater floor.

2. Geological Setting of the Séítah Formation

2.1. Geological Context

Jezero is a ∼45-km-diameter impact crater in the Nili Planum cratered highlands of Mars (Figure 1), straddling the western flank of the Isidis basin, which itself is an older giant impact structure of Noachian age (3.85–4.06 Ga; Schultz & Frey, 1990; Werner, 2009). The Mars 2020 rover *Perseverance* landed on the floor of Jezero crater on 18 February 2021, at the Octavia E. Butler landing site, tens of meters from the transition between two distinct geologic units exposed extensively on the crater floor (Farley et al., 2022). The olivine-bearing floor unit (Cf-f-1) (Goudge et al., 2015; Stack et al., 2020; Sun & Stack, 2020), which comprises the Séítah and Gaspé outcrops (Figure 1b), has been linked, based on spectral analysis, to a regional olivine-rich unit exposed near Jezero's crater walls, and across Nili Planum (e.g., Goudge et al., 2015; Kremer et al., 2019; Mandon et al., 2020; Sun & Stack, 2020). The Séítah formation (Cf-f-1) is exposed on the Jezero crater floor in irregularly shaped erosional windows through the Máaz formation (Cf-fr) (Figure 1b).

2.2. Rover-Based Observations of the Crater Floor Rocks

The *Perseverance* landing site was in the Cf-fr (Máaz formation), immediately east and north of an elongated exposure of the Cf-f-1 (Séítah formation), triangular in planform (Figure 2). This area is referred to as south Séítah (Sun et al., 2023). Morphologically, outcrops of the Séítah formation form a series of ∼1–10 m tall ridges that are oriented northeast-southwest and surrounded by sand dunes and coarser-grained regolith. The ridges contain rocks that show pronounced tabular layering of variable thickness (Bell et al., 2022; Beyssac et al., 2023; Farley et al., 2022). The rocks at ridge bases show cm-thick layering and are overlain by rocks, at the ridge tops, that show layering at a scale of ∼10–50 cm and are internally structureless.

The Séítah formation has been sub-divided into two members: the Bastide and Content members (Crumpler et al., 2023; Farley et al., 2022). The layered Séítah rocks have mostly been assigned to the Bastide member (Farley et al., 2022). Detailed observations of natural surfaces with Mastcam-Z and SuperCam RMI show that these layered rocks consist of densely packed crystals that are ∼1–3 mm in diameter, dark gray in color and have angular to sub-rounded shapes (Bell et al., 2022; Beyssac et al., 2023; Farley et al., 2022; Wiens et al., 2022). The grains/crystals have a clast-supported /phaneritic texture (Beyssac et al., 2023; Wiens et al., 2022). Lighter-toned material surrounds the dark gray grains. Observations of abrasion patches with WATSON show that the mm-diameter grains are light-toned and are equant or elongate in shape (Wogsland et al., 2023). PIXL and SuperCam and PIXL analyses show that these are olivine (Beyssac et al., 2023; Farley et al., 2022; Liu et al., 2022; Tice et al., 2022; Wiens et al., 2022). The layered rocks of the Bastide member are interpreted as olivine cumulate igneous rocks, based on their mineralogy and textures (Beyssac et al., 2023; Farley et al., 2022; Liu et al., 2022; Wiens et al., 2022). The emplacement origin of the olivine cumulates is poorly constrained; proposed emplacement mechanisms include: a large layered mafic intrusion, a thick lava flow, a lava lake, and an impact melt sheet (Beyssac et al., 2023; Farley et al., 2022; Liu et al., 2022; Wiens et al., 2022). The origin of the prominent layering observed in the Bastide member is not well understood but might represent primary magmatic layering in an olivine cumulate (Farley et al., 2022).

Locally, the Bastide member is overlain by pitted, structureless rocks that are not olivine-rich nor distinctly layered. These are assigned to the Content member of the Séítah formation (Beyssac et al., 2023; Udry et al., 2023; Wiens et al., 2022). The contact between the Content member and Bastide is not well-exposed throughout the area but shows a surface topography consistent with deposition over an irregular, possibly erosional, surface (Alwmark et al., 2023). The chemical compositions of Content rocks are similar to those of the Máaz rocks, that is, basalt, leading some authors to suggest that Content could be a basalt flow related to Máaz (Beyssac et al., 2023; Simon et al., 2023; Udry et al., 2023; Wiens et al., 2022). The crater retaining Máaz formation is widespread across the crater floor and consists of blocky, massive, and layered bedrock (Alwmark et al., 2023; Bell et al., 2022; Crumpler et al., 2023; Farley et al., 2022; Horgan et al., 2023; Udry et al., 2023; Wiens et al., 2022).

10.1029/2025JE009463

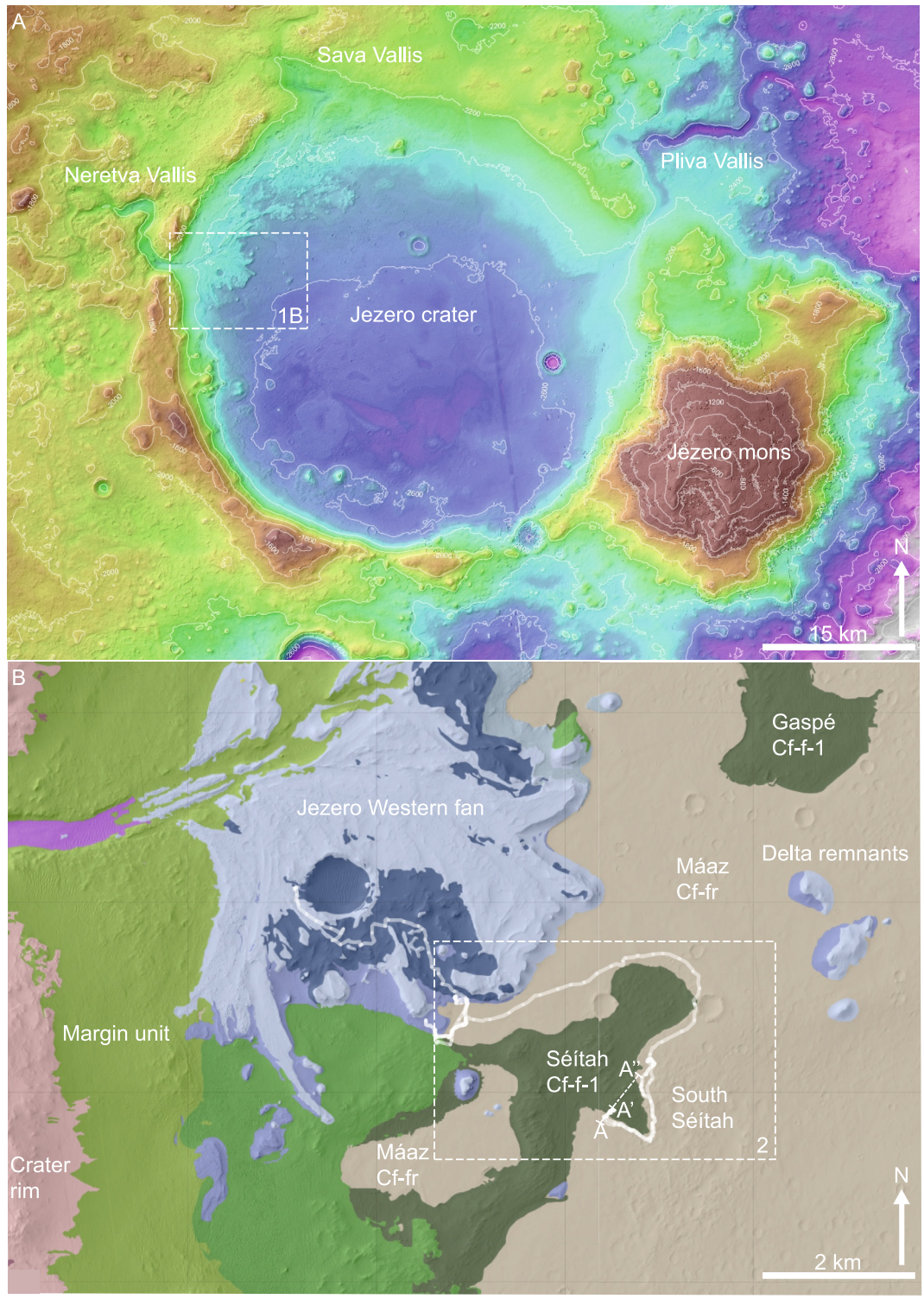

Figure 1. (a) CTX Digital Elevation Model (DEM) of Jezero crater; (b) Geological Map of western Jezero crater showing the outcrop extent of the crater floor lithologies (Sun & Stack, 2020) (Credit: NASA/JPL-Caltech/MSSS/UoA).

Máaz and Séítah rocks are exposed together along a 1 km long NE-facing escarpment, which comprises the contact between the two units, Artuby Ridge. At the southwestern margin of south Séítah (Figure 2), the Artuby ridge exposes well-layered outcrops of the lower members of the Máaz formation, informally named Rochette and

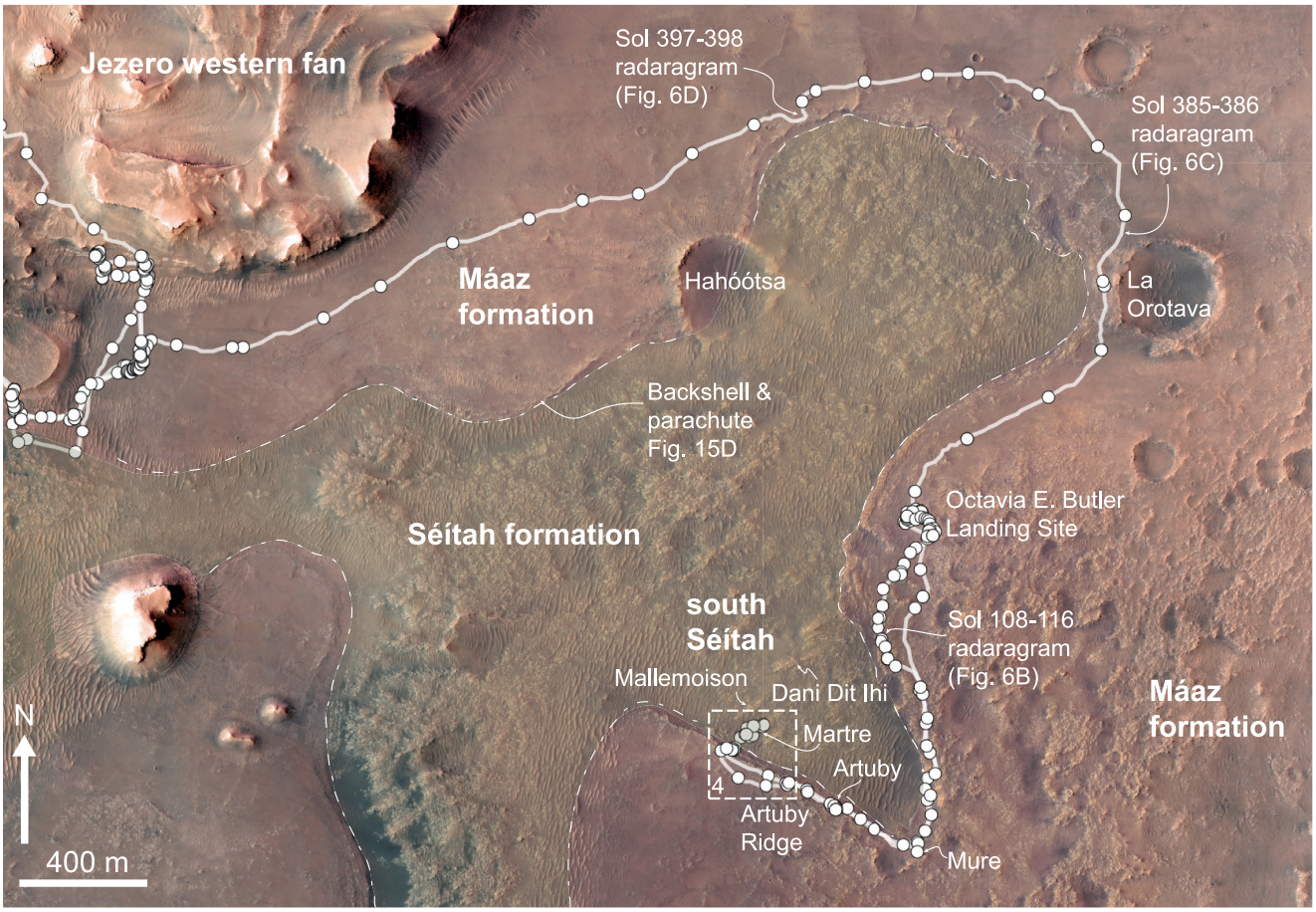

Figure 2. HiRISE orbital orthorectified image of the south Séítah region. The white line shows Perseverance's traverse around the Séítah inlier and the white dots show locations where the rover stopped. The location of the south Séítah transect, shown in more detail in Figure 4, is indicated by the dashed box. (Credit: NASA/JPL-Caltech/MSSS/UoA).

Artuby members (Crumpler et al., 2023). The lowermost Artuby member shows distinct layering with variable thickness, with mean values ranging between 7 and 74 mm (Alwmark et al., 2023), and a high degree of resistance to erosion. The overlying Rochette member appears as structureless rocks that cap the Artuby ridge and can be traced for hundreds of meters at the top of its scarp (Alwmark et al., 2023; Crumpler et al., 2023; Farley et al., 2022; Horgan et al., 2023).

The contact between the Artuby member of the Máaz formation and the Séítah formation lies at the base of the Artuby ridge, but is not exposed. From outcrop observations and RIMFAX ground penetrating radar (GPR) results, the Séítah formation bedrock clearly lies beneath Máaz formation rocks (Bell et al., 2022; Farley et al., 2022; Hamran et al., 2022; Thackston et al., 2024). GPR profiles show that layering in the lower Máaz members dips ∼10-15° to the southwest, perpendicular to the trace of Artuby ridge (Farley et al., 2022; Hamran et al., 2022). The obscuration of the Máaz—Séítah contact ensures that its nature (conformable vs. para-conformable vs. unconformable) remains elusive.

The upper members of the Máaz formation (Roubion, Naat'áanii, Ch'ał) are only present to the east of the Artuby ridge, where they form the surface of the CF-FR unit (Horgan et al., 2023). These members appear to fill in significant topography in this area, suggesting an erosional hiatus after the emplacement of the Rochette member (Thackston et al., 2024). The upper Máaz units exhibit a sharp truncation before reaching the Artuby ridge, potentially representing a flow front, and do not show the same degree of tilting as members exposed along the Artuby ridge. Based on these relationships, it was previously hypothesized that the deformation of Séítah and lower Máaz members along the Artuby ridge occurred between deposition of the lower and upper Máaz member

lava flows, and that the extent of the upper Máaz flows was controlled by the resulting topography (Horgan et al., 2023; Thackston et al., 2024).

3. Methods

3.1. Overview of Mastcam-Z Cameras and Images

The Mastcam-Z instrument is a pair of multispectral, zoomable, focusable cameras mounted on Perseverance's remote sensing mast (RSM), with a field of view ranging from 25.5° × 19.1° at 26 mm focal length to 6.2° × 4.2° at 110 mm (Bell & Maki, 2021). A calibration target is mounted on the rover's deck (Kinch et al., 2020). Each camera is equipped with an 8-position filter wheel, enabling multispectral imaging across 11 unique bands between 442 and 1,022 nm. Additional neutral density (ND) filters allow acquisition of true-color stereo views using a matched set of Bayer filters, while the full multispectral set includes an ND filter, a common 800 nm stereo filter, and five additional geology-specific narrow-band filters. The cameras have a stereo separation of 24.3 cm and a 2.3° toe-in between the boresights. This geometry enables stereo terrain models with ∼0.4 mm resolution at 2 and ∼1 m at 100 m (at 110 mm zoom, assuming 0.25-pixel correlation error), supported by calibration and geometric characterization (Hayes et al., 2021).

3.2. Stereo-Reconstruction of Mastcam-Z Images

Stereoscopy with Mastcam-Z enables the generation of 3D vision products, such as digital terrain models (DTMs), textured meshes, mosaicked panoramas, and other derived products. These products can be used for both visualization and quantitative geological and topographical analysis (Traxler et al., 2022). Image processing and stereophotogrammetry were performed using the known geometric parameters of Mastcam-Z and the known pointing angles of the RSM (Paar et al., 2016). The workflow consists of: (a) stereo matching to establish dense pixel correspondences from parallax caused by distance; (b) 3D triangulation to project parallaxes onto an infinite virtual cylindrical or spherical projection, producing a gridded surface model; (c) projection of image texture onto the grid; (d) fusion of adjacent stereo patches into a continuous 3D mosaic; (e) production of an Ordered Point Cloud (OPC) (Ortner et al., 2010; Paar et al., 2023). All calculations incorporate rover localization and orientation provided by the Mars 2020 Localization Teamlocalization team, together with pre-flight rover-to-camera geometric calibration. Minor pointing corrections are derived through point matching to compensate for small deviations from the original calibration (Hayes et al., 2021).

3.3. Data Visualization in PRo3D

3D visualization of rock outcrops was carried out using the Planetary Robotics 3D Viewer (PRo3D; Barnes et al., 2018), a software tool for viewing, annotating, and measuring geological features in processed Mastcam-Z OPCs within their correct spatial context. Out-of-core rendering allows interactive exploration of large 3D scenes by streaming geospatial data dynamically according to user navigation, with unseen data not rendered. Priority rendering enables the fusion of multiple OPCs by defining rendering order and facilitating integration of rover- and satellite-based data sets. PRo3D is optimized for geological analysis of OPCs, providing morphology-based tools to measure 3D distances and linear and planar orientations (e.g., lineation, fracture trends, bedding, and fracture dip/strike), and to digitize interpretations directly on the OPCs via their K-D Tree structure (Traxler et al., 2022). Annotations can be formatted by color and thickness to highlight semantic information. Contacts between lithologic units and internal layering can be traced with polylines, and their dip/strike data are hierarchically organized and analyzed relative to stratigraphic position (Barnes et al., 2018). These capabilities make PRo3D essential for deriving quantitative structural measurements from Mastcam-Z data and for placing outcrop-scale observations into their broader stratigraphic context.

3.4. Methods for Reconstructing Dips and Strikes and True Thickness of Layers

The primary geological analysis tools in PRo3D are the dip-and-strike tool and the true-thickness measurement tool. Dip and strike are determined by digitizing a polyline along a planar contact, followed by Principal Component Analysis (PCA)-based plane fitting (Barnes et al., 2018; Quinn & Ehlmann, 2019). This approach yields dip, dip azimuth, and strike calculations for each plane, together with residuals normal to the best-fit plane and estimates of maximum and minimum angular error. The resulting planes can be projected outward as discs, color-coded by dip magnitude, and visualized within PRo3D to assess their geologic reasonability in context with

the outcrop. These methods have previously been applied to stereo data from Mastcam images collected by the Mars Science Laboratory rover *Curiosity* (Banham et al., 2018, 2021) and by the Mars Exploration Rovers (Balme et al., 2017). The true-thickness tool allows users to connect two points and specify the dip and azimuth of a reference surface—typically the basal surface dip—to calculate the distance between points normal to that plane, providing a thickness measurement corrected for bedding inclination. Together, these tools enable quantitative measurement of bedding geometries as well as layer and unit thicknesses directly from Mastcam-Z stereo data, forming the basis for structural analysis of the Séítah dome.

3.5. Methods and Assumptions Used for Cross-Section Construction

We use dip measurements collected from the present-day topographic surface to extrapolate surface observations to the subsurface, characterize structural geometry and derive a formation or deformation process. We maintain the assumption of constant thickness as we found no evidence for or against this postulate. The assumption of constant layer thickness enables construction of a testable model of the Séítah-Máaz relationship. To construct this model, we used the bisecting kink-band technique (Mitra & Marshak, 1988), which assumes that dips change over short distances (across axial surfaces) and thus form domains or panels of constant layer dip, separated by angular hinges. We did not directly observe angular hinges in outcrop data, but we did observe planar layer geometries as opposed to more rounded geometries. In our model, the kink-bands bisect the dip values of the dip domains they bound to preserve layer thickness between those dip domains. This is a geometric technique ensures that line lengths are preserved and does not consider the layers' mechanical responses to deformation. We did not observe any of these hinges or kink-bands in the outcrop, so we have maintained the kink band to bisect the dip domains it borders.

4. Topography of the Séítah and Gaspé Domes

The Séítah formation comprises two main crater-floor outcrops with elongate planforms and lobate margins (Stack et al., 2020). South Séítah is near the fan's southeastern edge and trends NE–SW (Figure 2; Farley et al., 2022) and was the focus of Perseverance's ground investigation. The other, informally named Gaspé, lies north of the western fan and trends NW–SE. Although orbital and rover observations show that the Máaz formation stratigraphically overlies Séítah (Farley et al., 2022; Hamran et al., 2022; Horgan et al., 2023), Séítah terrain is consistently elevated relative to the surrounding flat Máaz lava plains. To quantify this geometry, we analyzed HiRISE digital elevation models (DEM; ∼1 m/px) for both domes (Figure 3).

The Séítah dome covers an area of ∼4.62 km^2; elevation spans a range from −2592 to −2531 m (61 m). The highest elevation topography runs approximately north-south along the western half and decreases to the northeast and south-eastward, with the lowest elevations in the south Séítah lobate extension. The Gaspé dome covers an area ∼3.50 km^2 and shows an elevation ranging from −2569 to −2515 m (54 m). The highest topography occurs in the center of the inlier, decreasing abruptly to the NE and SW margins and toward the SE of the elliptical body. The mean elevation for Séítah is −2559 ± 1 m and Gaspe has a mean that is ∼9 m higher at −2550 ± 10 m. The elevations of the contact between the Séítah and Máaz formations vary slightly from the surface expressions of the topography. The contact in the Séítah dome ranges from −2590 to −2549 m (41 m), while the contact in Gaspé ranges from −2568 to −2532 m (36 m). These figures represent systematic underestimates of the structural elevation of key reference surfaces, such as the Séítah–Máaz contact. However, even with this downward bias, the Séítah formation occupies a higher topographic position than Máaz in the Séítah and Gaspé domes, contrary to their stratigraphic relationship. To place this observation in context, we derive a structural model constrained by detailed measurements of the Séítah and Máaz formations along the south Séítah transect, allowing us to define the true structural geometry of a part of south Séítah, which we can apply to the rest of the Séítah and Gaspé domes.

5. Structural Analysis of the South Séítah Dome

5.1. Visualization of Digital Outcrop Geometries in the Séítah Formation

To reconstruct the structural geometry of the Séítah dome, we analyzed Mastcam-Z mosaics and OPCs across the south Séítah transect (Figure 4). A topographic profile showing the locations of the outcrops that form the transect from the Artuby ridge in the SW to the Caille outcrop in the NE, is shown in Figure 4. We present the outcrop analyses in sequential order from southwest to northeast. The Mastcam-Z OPCs covering the key outcrops were

10.1029/2025JE009463

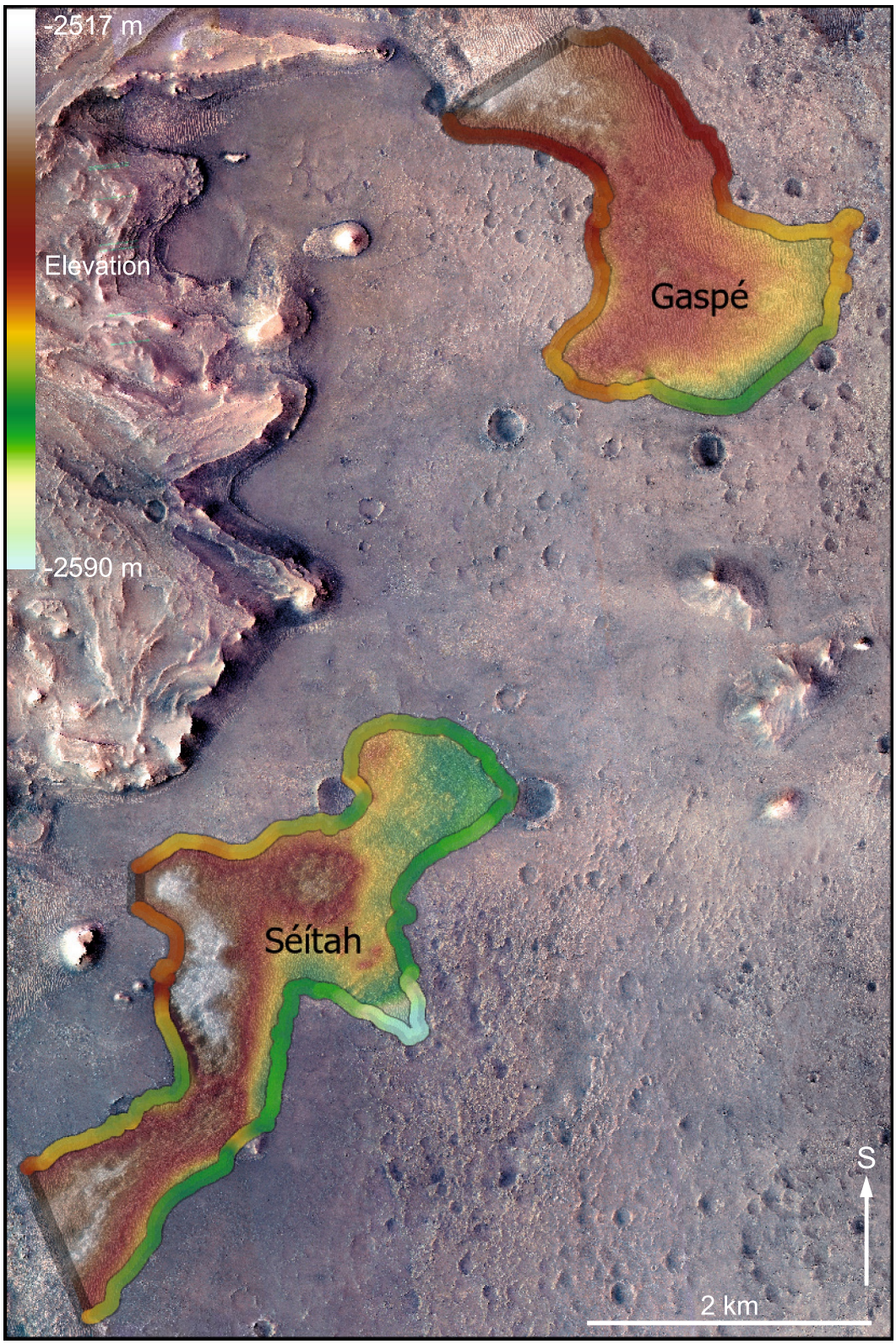

Figure 3. HiRISE color mosaic of Jezero crater with overlain Séítah and Gaspé colorized topography. Séítah has an elevation range of −2,592 to −2,530 m, while Gaspé has a range of −2,515 to −2,569 m (total ranges of 62 and 54 m, respectively). Elevation of the outer edge of these units is enlarged at the same color scale to highlight the elevation range of the contact between the CF-f-1 and CF-fr units. Overall, the topography of Séítah and Gaspé is higher than the surrounding Maaz formation, while the contact between the two shows a consistent trend with higher elevations in the west/northwest and lower elevations to the east/southeast (Credit: NASA/JPL-Caltech/MSSS/UoA).

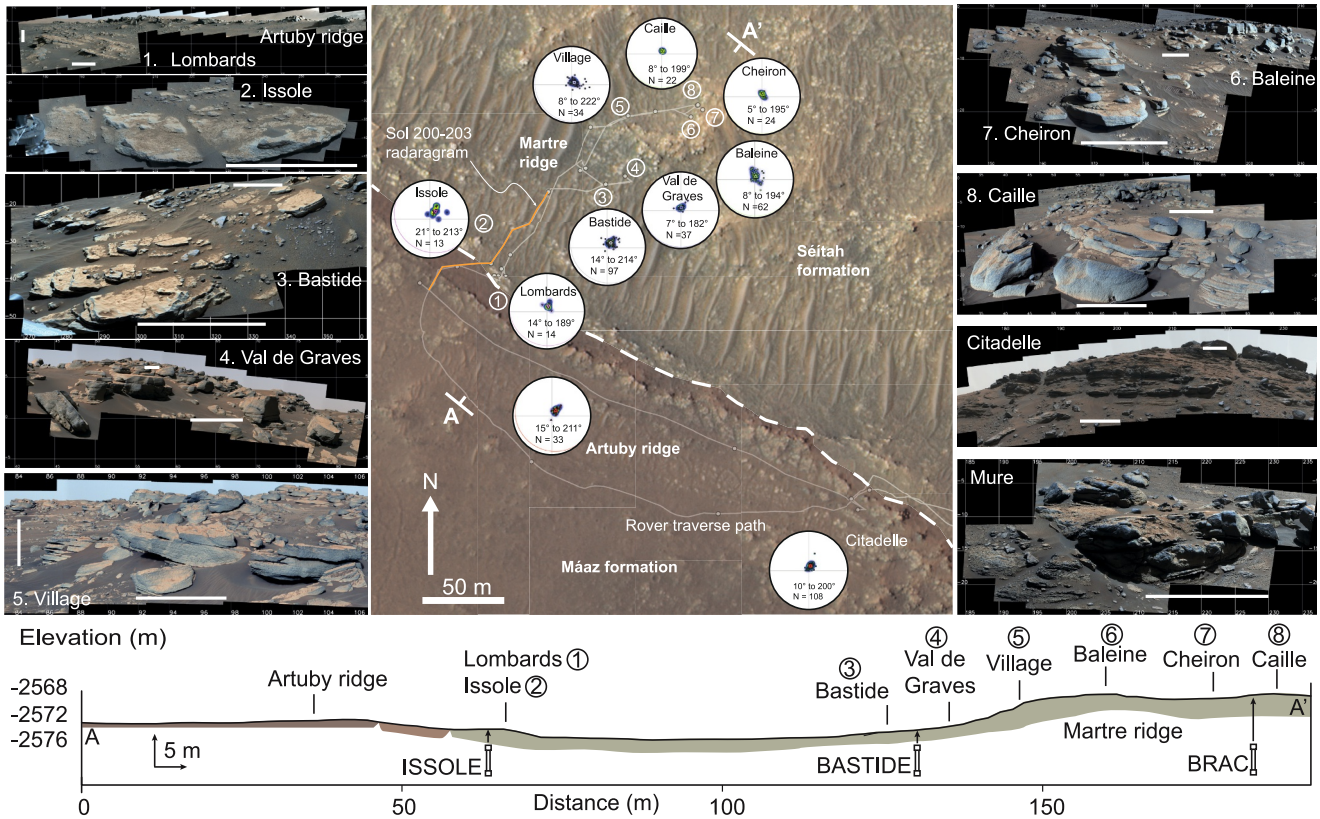

Figure 4. Geological context, outcrop panoramas, and topographic profile of the Séítah–Máaz contact zone explored in the south Séítah transect. The central map shows the rover traversing across the Martre and Artuby ridges within the Séítah and Maaz formations, respectively, with the location of the Sol 200–203 radargram highlighted in orange (radargram ashown in Figure 6a). Numbered circles mark investigated outcrops (1–10), with representative stereonets of the dip data for each outcrop presenting the poles to the measured layer dips, showing the mean orientation at each outcrop. Panels surrounding the map show rover mosaics of each site: 1. Caille (Sol 240 zcam08264), 2. Cheiron, 3. Baleine (both Sol 240 zcam08263), Val de Graves (Sol 205 zcam08231), Bastide (Sol 205 zcam08232), Village (Sol 211 zcam08246), Lombards (Sol 211 zcam08246), Issole (Sol 290 zcam08314), Artuby ridge (Sol 211 zcam08246), Citadelle (Sol 342 zcam08367) and Mure (Sol 169 zcam08181). The lower panel presents the A–A′ topographic profile across the study area, along which the cross-section reconstruction in this work was carried out, highlighting relief variations between the Séítah and Máaz formations and the positions of key outcrops along the transect. Scale bars on the mosaics are ∼1 m long. (Credit: NASA/JPL-Caltech/MSSS/ASU/UoA).

integrated with HiRISE DTM and orthorectified images (ORIs) to build digital outcrop models. From these, we extracted layer dimensions and orientation data (strikes and dips) to constrain the three-dimensional geometry of the Séítah formation and to document variations in outcrop character with stratigraphic position. Stereonets of the derived dip measurements from each outcrop are shown alongside the transect in Figure 4, together with images of the outcrops they were collected from. We used these dips to adjust layer thickness calculations at each outcrop and the statistical spread of these values is illustrated in the box and whisker plots in Figure 5. Here we present results from Máaz formation outcrops in the southwestern part of the transect, toward Séítah formation outcrops northeast of the Artuby ridge, documenting the transition and systematic geometrical variations therein. The results are summarized in Table 1. Structural observations at the surface were complemented with the RIMFAX radargrams shown in Figure 6, which were collected during rover traverses on sols 200–203 (location in Figure 4), 108–116 and 385–396 (locations in Figure 2a).

5.2. Structural Geometry at the Southwest Margin of the South Séítah Dome

At the southwestern end of the south Séítah transect, sub-horizontal beds of the Máaz formation emerge through regolith cover at a low point adjacent to the southwest flank of the Artuby ridge (Figure 7a; location of Artuby ridge in Figure 4). We did not obtain quantitative dip measurements of these layers, but any exposed layers away from the Séítah-Máaz contact do not show any signs of measurable dip, an observation consistent throughout the Máaz formation. The Artuby ridge is capped by the resistant layers of the Rochette member of the Máaz formation

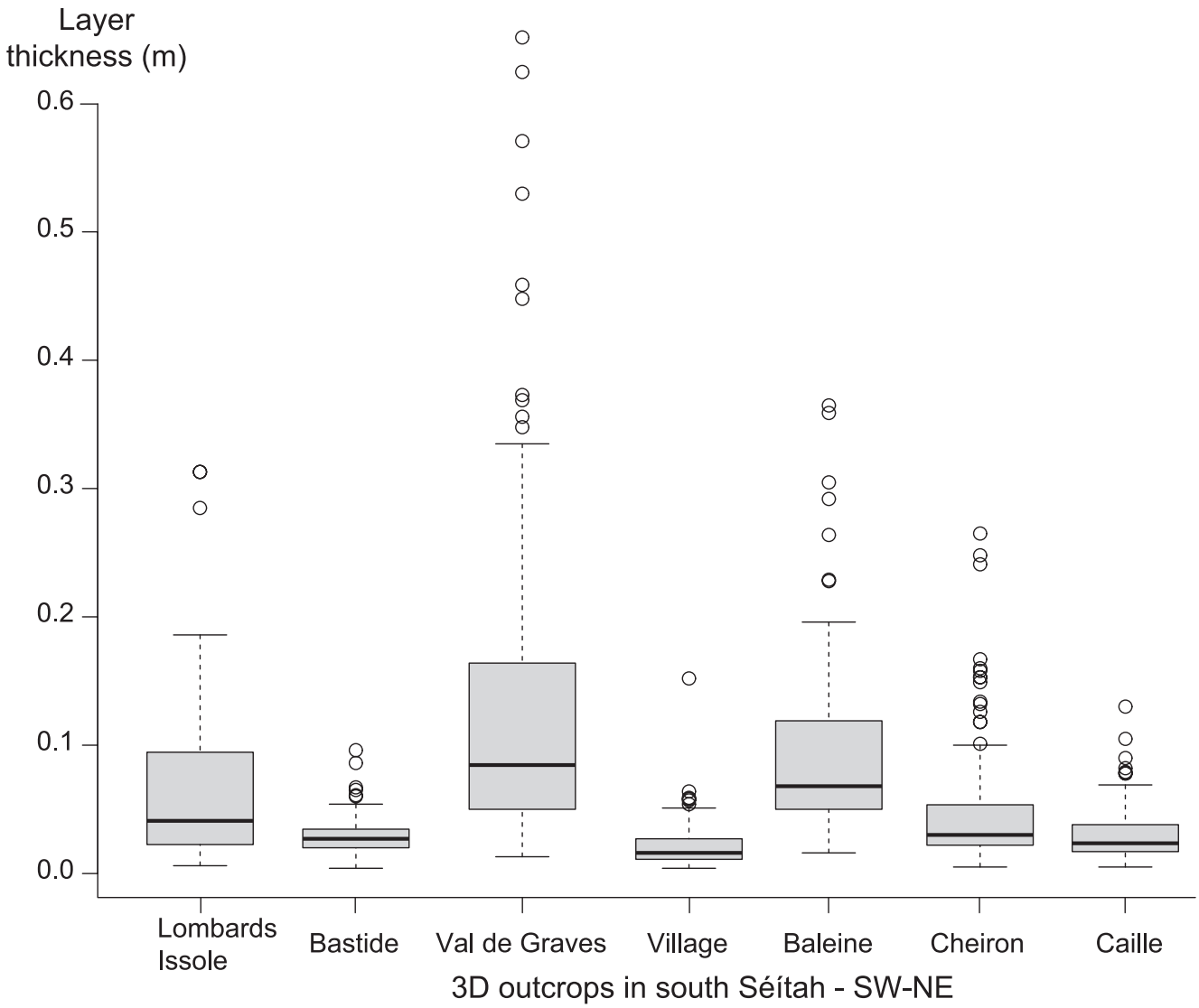

Figure 5. Distribution of layer thickness across seven 3D outcrops within the south Seitah transect. Boxplots show the interquartile range (IQR) for each outcrop, with horizontal lines indicating median thickness and whiskers extending to 1.5 × IQR. Circles represent outliers. Layer thickness generally ranges from near zero to ∼0.6 m, with most values below 0.2 m. Val de Graves exhibits the greatest variability and thickest layers, while Caille, Village, and Bastide display relatively thin and uniform layers.

(Figure 7). Thirty-three dip/strike measurements collected along ∼100 m of the ridge close to the boundary with the Séítah formation yield a mean plane dipping 15° toward 211° (inset stereonet, Figure 8a).

Outcrops at the base of the Artuby ridge, stratigraphically below the Máaz formation rocks, expose the transition between the Séítah and Máaz formations. The base of the ridge is formed by the Issole and Lombards outcrops, which comprise olivine-rich Séítah formation rocks. The Lombards outcrop, consists of alternating recessive and resistant layers. Fourteen measurements gave a mean plane dipping 14° toward 189° (Figure 8a). Nearby, the Issole outcrop (Figures 6b and 6c) comprises layered Séítah rocks, where 14 dip/strike measurements yield a mean plane dipping 21° toward 213° (Figure 8b). Layering is poorly preserved, producing a wide spread of values in the stereonet. Basal layer dip 10–20° toward ∼215°, while thinner upper layers steepen to 30–35°. Layer thicknesses at Lombards are typically 80–100 mm, with thicker layers up to 200–300 mm (outliers in Figure 5), suggesting numerous thin layers interfingered with more massive layers. Combining Issole and Lombards data gives a mean layer thickness of 72 mm, a median of 41 mm, and an interquartile range of 23–95 mm (Figure 5), consistent with textures seen in image mosaics (Figure 7b). Dip and dip azimuth measurements at the Lombards

Table 1
Summary of Bedding Orientation and Layer Thickness Measurements From Key Outcrops

Outcrop	Number of Data Points	Minimum Dip (°)	Maximum Dip (°)	Mean Dip (°) Spherical	Mean Strike (°) Spherical	Vector Strength Spherical	Mean Dip (°) Circular	Mean Dip Azimuth (°) Circular	Dip Vector Strength Circular	Mean Strike (°) Circular
Lombards	14	9	25	14	105	0.93	13	195	0.93	105
Issole	13	9	39	24	125	0.91	22	215	0.91	125
Bastide	97	5	32	16	127	0.9	14	217	0.9	127
Val de Graves	37	1	26	9	88	0.83	8	179	0.83	89
Village	124	1	39	12	133	0.77	10	224	0.77	134
Baleine	62	2	26	17	105	0.64	11	195	0.63	105
Cheiron	24	1	13	9	121	0.73	6	211	0.73	121
Caille	22	5	12	8	106	0.96	7	196	0.96	106
artuby	108	0	38	12	108	0.9	11	198	0.9	108
Mure	53	2	41	29	101	0.5	14	191	0.45	101

Outcrop	Number of Layers	Minimum Thickness (m)	Maximum Thickness (m)	Mean Thickness (m)	Median Thickness (m)	Standard Deviation Thickness (m)
Issole and Lombards	51	0.006	0.313	0.072	0.041	0.074
Bastide	115	0.004	0.096	0.03	0.027	0.015
Val de Graves	102	0.013	0.652	0.136	0.085	0.138
Village	209	0.004	0.152	0.02	0.016	0.015
Baleine	109	0.016	0.365	0.092	0.068	0.067
Cheiron	139	0.005	0.265	0.048	0.03	0.047
Caille	152	0.005	0.13	0.03	0.023	0.019

Note. (a) Stereonet-derived dip and strike statistics for each outcrop, including spherical and circular mean values and vector strengths. (b) Thickness statistics for individual layers at each outcrop, showing minimum, maximum, mean, median, and standard deviation values.

and Issole outcrops in the Séítah formation are approximately concordant with values in the directly overlying Máaz formation outcrops in the northwest end of the Artuby ridge.

5.2.1. Subsurface Data at the Southwestern End of the South Séítah Transect

RIMFAX data was collected in the south Séítah transect part of the traverse crossing the Séítah-Máaz boundary between sols 200–203 (Figure 6a) and reported by Hamran et al. (2022). The transect was almost perpendicular to the strike of the strata in the area and provides important data on the sub-surface geometry (Hamran et al., 2022; Thackston et al., 2024). The Séítah-Máaz boundary observed at the surface at the Artuby ridge was plotted on the Sol 200–203 radargram, showing that the Séítah formation strata driven over in sols 201–203 are dipping in the same direction as that measured at the surface, and continue to some depth beneath the Máaz formation.

5.3. Martre Ridge

In the south Séítah area of the Séítah dome, Séítah formation rocks are exposed in a series of NE-SW-oriented sub-parallel ridges, examples of which include the Martre, Dani Dit Ihi and Mallemoisson ridges (Figure 2). These ridges are ubiquitous throughout the exposed part of the Séítah formation and are likely the result of aeolian erosion of more extensive exposures of Séítah formation rocks. *Perseverance* investigations of the South Séítah dome focused on one of these ridges, the NE-SW-trending ∼170 m long and ∼55 m wide Martre ridge, which shows up to 3 m of topographic relief in relation to the surrounding south Séítah rocks. The highest elevation point of the Martre ridge is approximately 6 m higher than the base of the Máaz formation at the Artuby ridge. The outcrop character and the locations on the Martre ridge are shown in Figure 9. Below we describe the outcrop

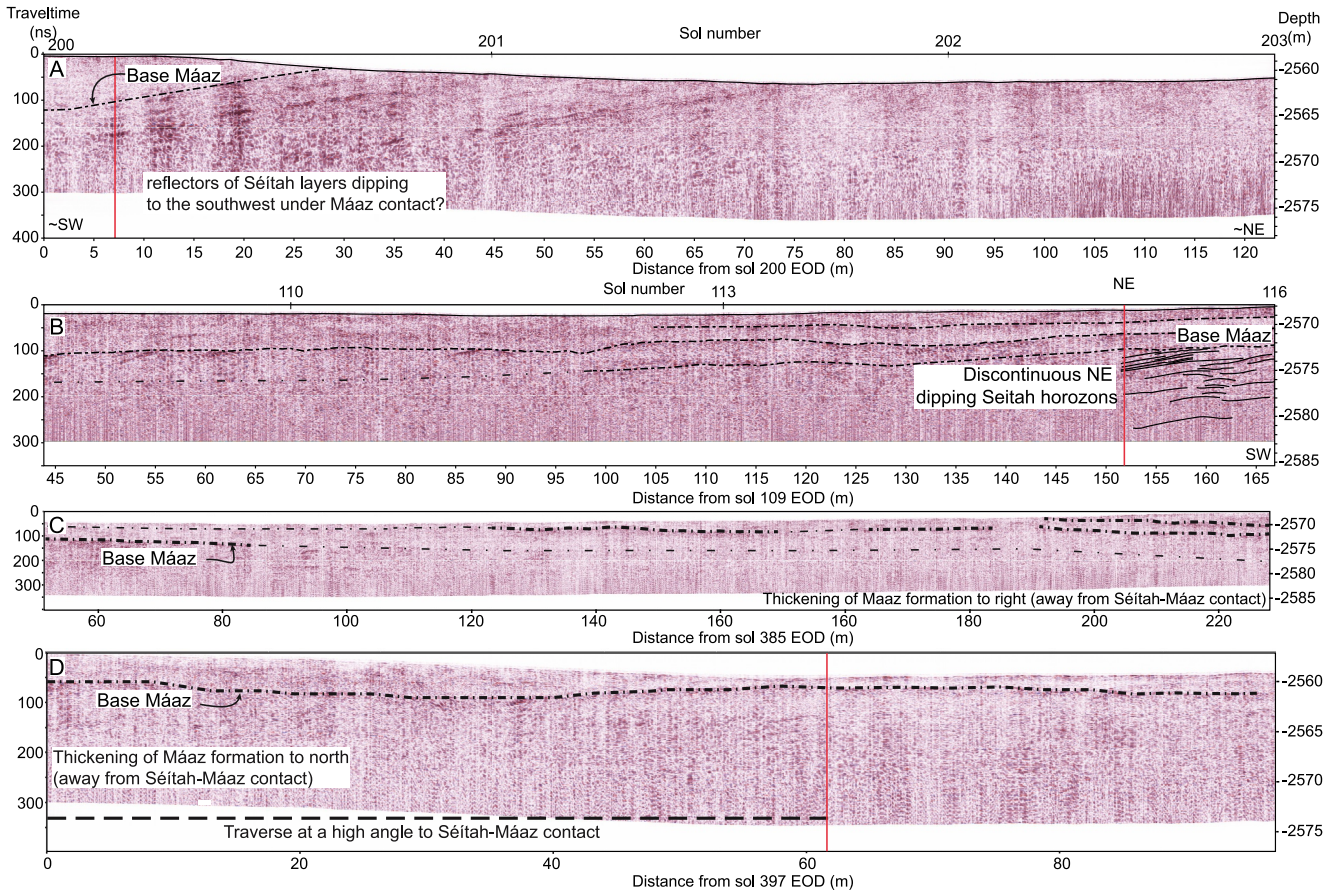

Figure 6. RIMFAX radargrams acquired along segments of the rover traverse crossing the Séítah–Máaz contact at relatively high angles. Locations of these traverses are shown in Figure 2 and the Supporting Information S1. (a) Sols 200–203: beginning of the south Séítah transect (Figure 4), showing southwest-dipping reflectors beneath the Máaz contact. (b) Sols 108–116: northeastern side of south Séítah (Figure 2), with discontinuous northeast-dipping horizons within Séítah to the right of the red line, where the traverse was approximately perpendicular to the contact. (c) Sols 385–386: thickening of the Máaz formation away from the contact (Figure 2). (d) Sol 398: traverse at a high angle to the contact, showing further thickening of the Máaz formation to the north (Figure 2). (Credit: NASA/JPL-Caltech/University of Oslo).

geometry in different sectors of the Martre ridge. We analyzed the outcrops in Figure 9 at the southwest (Figure 9a) and northeast (Figures 9b and 9c) ends of the ridge. Compiling image data from multiple sols into digital outcrop models allowed us to trace and project stratigraphy across poorly exposed areas (Figure 9d), improving stratigraphic correlation along the transect and enhancing subsurface interpretation.

5.3.1. Southwest Martre Ridge

At the southwest end of the Martre ridge, a series of Séítah outcrops record systematic changes in dip and variation in bedding thickness. The Bastide outcrop, forming the lowermost exposed Séítah layers at the base of the Martre ridge (Figure 4), consists of flagstone-like, erosion-resistant outcrops with well-developed planar parallel layering (Figure 10a). Ninety-seven dip measurements yield a mean plane dipping 14° toward azimuth 214° (Figure 10a). Layer thicknesses ranged from 4 to 96 mm, with a mean of 30 mm, a similar median of 27 mm, and a standard deviation of 15 mm (Figure 5), consistent with the thin layering with minimal variation in layer thickness seen outcropping in this part of the Séítah formation.

Directly upslope from Bastide, the Val de Graves outcrop exposes blocky, well-layered Séítah rocks (Figures 8a and 9b). Thirty-seven dip measurements cluster about a mean plane dipping 7° toward 182°, with outliers dipping 19–24° toward ~220°, possibly reflecting local variations, fractures, or displaced blocks. The consistently shallower dips at Val de Graves relative to Bastide indicate a transition between dip domains (Figure 9a). Layer thicknesses are significantly greater and more variable than at other Martre ridge sites: 102 measurements ranged from 13 to 652 mm, with a mean of 136 mm, a median of 85 mm, and a standard deviation of 138 mm. The

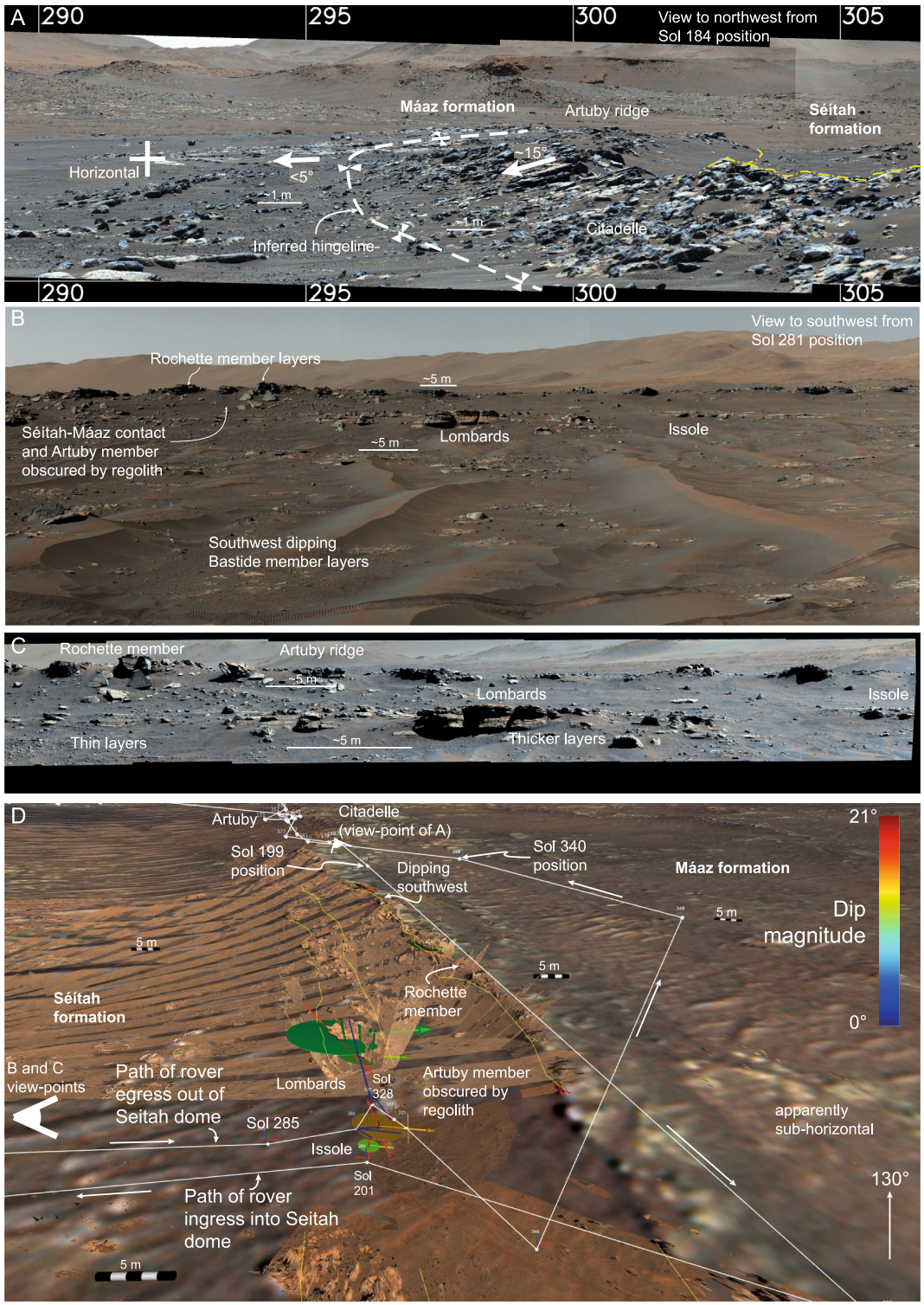

Figure 7. (a) View of the dipping Máaz layers in Artuby ridge as seen looking south from Citadelle, and the flatter lying Máaz to the southwest (Sol 282 zcam08301); (b) Mastcam-z110 mosaic of the Issole, Lombards and Artuby ridge layers (Sol 282 zcam08303); (c) Mastcam-Z mosaic looking toward the southwest end of the south Séítah transect (Sol 184 zcam08202); (d) View of a 3D reconstruction of the Seitah-Maaz contact in Pro3D showing HiRISE DTM and orthorectified image data overlain by Mastcam-Z stereo-image data. The rover traverse path is indicated by a white line with associated sol labels and the main mapped stratigraphic boundaries are represented by yellow lines. A subsample of dip and strike measurements is shown using colored disks with red strike lines and dip azimuth arrows. Dip disks are color coded by dip magnitude. Black and white scale bars are 5 m (Credit: NASA/JPL-Caltech/ASU/UMSSS/Joanneum Research/VRVis).

interquartile range (51–163 mm) is the broadest of any outcrop analyzed in south Séítah (Figure 5). This variability is consistent with the more structureless appearance of layering compared to Village and Bastide, and the thicker layering as it appears in outcrop. Val de Graves occupies the topographically highest part of the ridge and likely represents the upper Séítah formation.

Approximately 40 m northeast along the Martre ridge from Val de Graves, the Village outcrop (Figures 4 and 10c) exposes well-developed layering. Thirty-four dip measurements yield a mean plane dipping 8° toward azimuth 222° (inset stereonet, Figure 10c), similar to Val de Graves, though several layers dip more steeply, 20–38° westward (red disks in Figure 10c). We obtained 209 thickness measurements ranging from 4 to 152 mm with a median which is half of that at Bastide at 16 mm, but shows comparable mean values to that at the outcrop of 30 mm. The standard deviation (15 mm) is lower than at Val de Graves, but identical to that at Bastide, indicating reduced variance in layer thickness at Village and Bastide together with the overall thinner layers (Figure 5).

5.3.2. Northeast Martre Ridge

The northeastern end of the Martre ridge, is the farthest extent of the south Séítah transect, comprising the Baleine, Cheiron and Caille outcrops (Figures 4, 9 and 11). Mastcam-Z mosaics of the Caille area show ridges and promontories formed of gently southwest dipping, blocky, thickly layered Bastide member rocks. Content member outcrops are distributed at various elevations. Lower ridges and intervening ground consist of buff-to gray-weathering, thin but well-preserved layers (Figures 9b and 9c).

At the southwest end of the ridge adjacent to Village on the transect (Figure 4), the Baleine outcrop (Figure 11a) forms a ∼10-m-long SW–NE scarp up to 1 m high, composed of thick structureless beds that pinch out at both ends. The outcrop shows discontinuous geometry comparable to that of Cheiron, with a smooth-textured lithology forming the scarp and rough-textured, granular material beneath. Bedding is generally gentle, with 62 measurements yielding a mean dip of 8° toward 194° though values range from sub-horizontal to ∼26°. The wide circular standard deviation (∼55°) reflects deviations from the dominant south-southwest dip due to irregular, non-planar layer geometries. Baleine layers are thicker than at Caille, ranging from 16 to 365 mm, with a mean of 92 mm, a median of 68 mm, and a standard deviation of 68 mm (Figure 5). Layer thicknesses at Baleine are more comparable to those at Val de Graves.

Northeast of Baleine lies the Cheiron outcrop (Figure 11b). Twenty-four dip measurements yield a mean dip of 5° toward 195° though the stereonet shows variability reflecting the discontinuous layering observed in the outcrop. Thin beds transition downwards into a rough-textured, granular lithology. Layer thicknesses span 5–265 mm, with a mean of 48 mm, a median of 30 mm, a standard deviation of 47 mm, and an interquartile range of 22–54 mm (Figure 5), slightly broader than at Caille, Village and Bastide, but with similar median values. The higher mean value and standard deviation with respect to Bastide and Village implies that there are more thicker layers in the outcrop, and these occur toward the topographically higher parts of the outcrop. In the low-lying ground between Caille and Cheiron, Content member rocks overlie Bastide strata though this contact is not resolved in 3D models of the Cheiron outcrop.

The northeastern extent of the Martre ridge hosts the Caille outcrop (Figure 4), which is a ∼1.5 m thick section of well-layered Bastide member rocks. A mean dip of 8° toward azimuth 199° was calculated from 22 dip measurements. Layer thicknesses ranged from 5 to 130 mm, with a mean of 30 mm, median of 24 mm, and standard deviation of 20 mm. The boxplot in Figure 5 shows an interquartile range of 17–38 mm, comparable to Bastide and Village but with higher mean values, as shown at Cheiron. Overlying the Bastide strata are structureless, pitted Content member rocks. The basal Content contact was moderately well exposed; two measurements agreed on a dip of 12° toward 119° (Figure 11c). This orientation is slightly discordant with dips in underlying Bastide member strata, and the distribution of Content rocks does not strictly follow the Séítah formation geometry (Figure 9c).

Taken together, the Baleine, Cheiron and Caille, outcrops document gently southwest-dipping Bastide member strata with down-section decreasing layer thickness, and relatively consistent dip magnitude, between 5°–8° to the southwest, capped locally by discordant Content member rocks.

5.4. Summary of Structural Geometry in the South Séítah Transect

Across the South Séítah transect, bedding consistently dips southwest but varies systematically in magnitude, thickness, and geometry. At the southwest margin (Issole–Lombards–Artuby; Figures 4, 7, 8, and 12), dips are

10.1029/2025JE009463

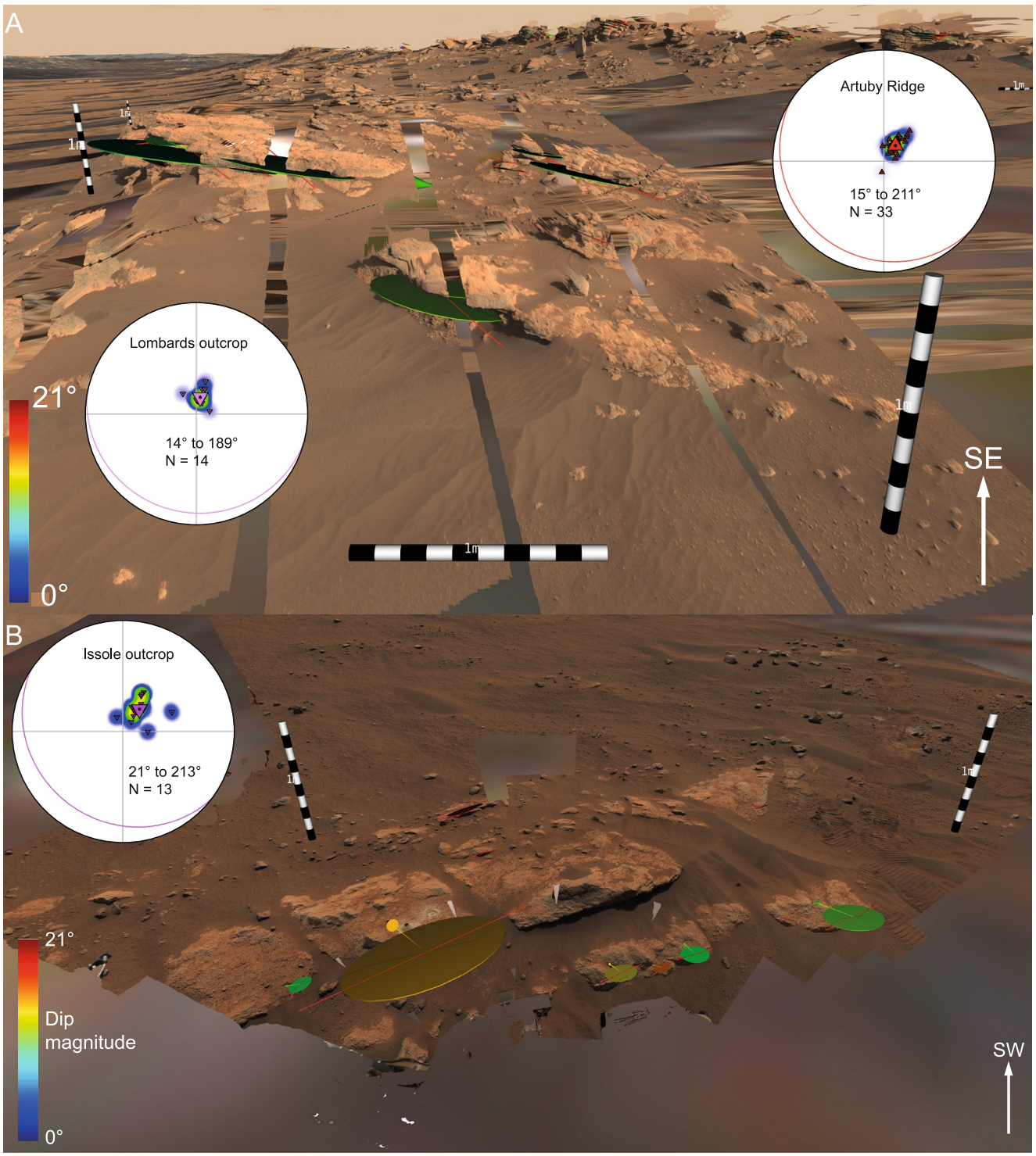

Figure 8. Mastcam-Z OPCs of outcrops at the NE base of the Artuby ridge visualized in PRo3D, showing the dips measured as disks colored by dip magnitude. The inset lower hemisphere equal area stereonets show the spread of layer orientations at each outcrop plotted as poles to the planes. Scale bars are 1 m. (a) Lombards; (b) Issole (Credit: NASA/JPL-Caltech/ASU/MSSS/Joanneum Research/VRVis). See Supporting Information S1 for image mosaic details.

steeper (between 10 and 35° averaging 17° toward ~210–215°) and layering is thin (median ~41 mm; Figure 5). At the southwest Martre ridge (Bastide–Val de Graves–Village; Figures 9–11), dips shallow from ~14° at Bastide to ~7–8° at Val de Graves and Village, coinciding with a shift from thin, regular beds (median 27 mm at Bastide)

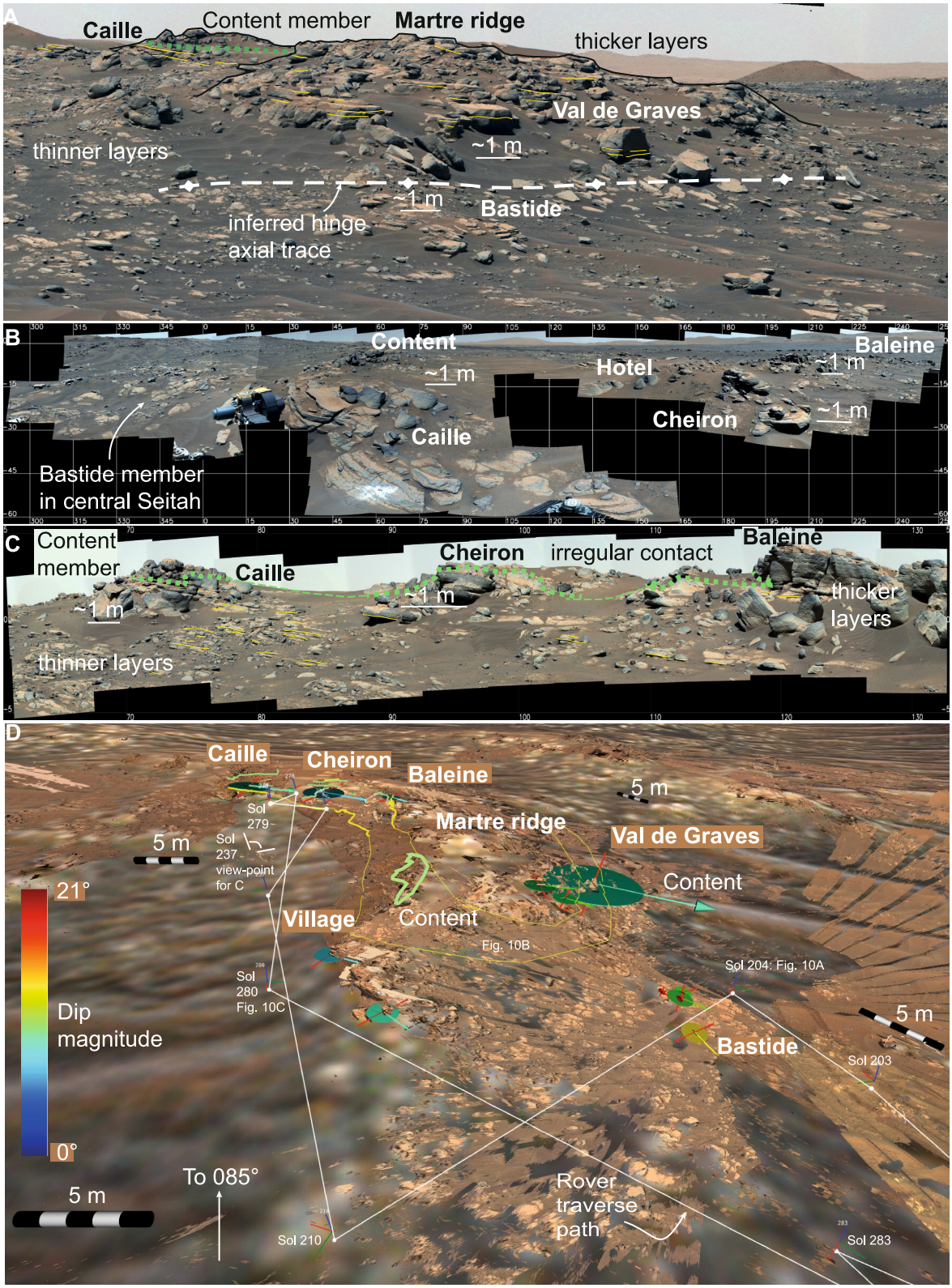

Figure 9.

to thicker and more variable units (median 85 mm at Val de Graves). At the northeastern end (Caille–Cheiron–Baleine; Figures 8 and 10), dips remain gentle (5–8° toward ~195–200°) but layering is increasingly irregular and thicker, with median values increasing up-section, from 24 mm at Caille to 68 mm at Baleine (Figure 5). Discordant Content rocks locally overlie Bastide strata in this northeastern area (Figure 9).

5.5. Along-Strike Structure of the Máaz Formation

Having established the structural geometry perpendicular to dip, we now examine the along-strike geometry of the Séítah–Máaz contact to assess lateral changes in the structural geometry. Along the southwest facing side of the Artuby ridge, two key outcrops record the structure of the Máaz formation along the contact of Artuby and Mure (See SI part S1 for mosaic details). The Citadelle outcrop (Figure 12a) exposes the Artuby member in three main exposures. The largest reveals a ~2.9 m thick section of granular, layered rock. Persistent planar beds can be traced more than 10 m along-strike. We collected 108 layer orientations from these outcrops, producing a mean plane dipping 10° toward 200°.

At the southeastern extent of south Séítah, the Mure outcrops (Figure 12b, location in Figure 2) expose upper members of the Máaz formation, potentially including Roubion, Rochette, and Naat'áanii member rocks (Crumpler et al., 2023; Horgan et al., 2023). Outcrops are well-layered but display greater variability in dip than other Máaz sites. Layers show variable thicknesses and lenticular geometries (Figure 12b), with overlying layers draping across underlying topography, likely a manifestation of their emplacement as lava flows. This draping produces dispersed strike and dip values though 47 measurements cluster around a mean dip of 2° toward 194°. This low dip indicates an along-strike decrease in dip magnitude, from 10 to 15° at Artuby to near-horizontal at Mure.

5.6. Séítah Dome Geometry Away From the South Séítah Transect

5.6.1. Central Section of the South Séítah Dome

Whilst *Perseverance* was unable to traverse into the central sections of south Séítah, long distance views to the north from the Séítah-Máaz contact (Figures 13a and 13b) reveal sub-horizontal layering within the Mallemoison and Dani Dit Ihi ridges. Here, layered slabs of Séítah rocks appear comparable to outcrops of Bastide member rocks (as shown on Martre ridge in Figure 13c) with sub-horizontal (<5°) apparent dips. Measurement of true dips and strikes was impossible because the ridges were too distant.

5.6.2. Northeast Margin of South Séítah

The northeastern side of south Séítah (on the opposite side the area of the transect) was visited between sols 108 to 130 (Figure 2). Mastcam-Z mosaics taken from the northeastern side of south Séítah show its main outcrops to the southwest (Figure 14) but are not useful for extracting layer orientations because of poorly exposed rock and non-ideal viewing geometries. However, some layer orientations can be approximated (Figures 14b and 14c), thereby constraining the relationship between Séítah and Máaz in this location. The mosaic in Figure 14a was taken when the rover was sitting on the Máaz formation, which forms the foreground of the image. Layering is not as well preserved in this region as in the south Séítah transect, but several outcrops of the Séítah formation are observed to dip toward the view-point. It is not possible to measure dips directly, but we can qualitatively deduce that the Séítah formation dips shallowly to the northeast, as shown in the blown-up parts of the Sol 117 mosaic in Figures 14b and 14c.

Figure 6b shows a RIMFAX radargram obtained between sols 108–116 on the northeastern side of the south Séítah outcrop. During these sols, the traverse was doglegged, but the final ~15 m toward the Sol 116 end-of-

Figure 9. (a) The southwest end of the Martre ridge imaged on Sol 201, showing the locations of the Bastide, Val de Graves, Content and Caille outcrops in context with each other (Sol 201 zcam08219). The location of a surface axial trace of defined by a change in overall dip magnitude is highlighted with the dashed white line; (b) Mastcam-Z z34 mosaic collected between sols 255 and 265 (zcam08278-08283) showing the Caille, Cheiron and Baleine outcrops and the surrounding terrain at the northeast end of the transect at south Séítah; (c) The Caille, Cheiron and Baleine outcrops viewed along strike on Sol 238, providing a clear view of stratigraphic relationships (Sol 238 zcam08261); (d) Mastcam-Z stereo-image data processed into Ordered Point Clouds and viewed with HiRISE topography and image data in Pro3D, together with digitization of the mapped stratigraphic contacts as green and yellow lines. A subsample of representative dip and strike measurements is shown as colored disks with red strike lines and dip azimuth arrows. Dip disks are color coded by dip magnitude following the inset color ramp. Scale bars are 5 m (Credit: NASA/JPL-Caltech/ASU/UoA/MSSS/Joanneum Research/VRVis). See Supporting Information S1 for image mosaic details.

10.1029/2025JE009463

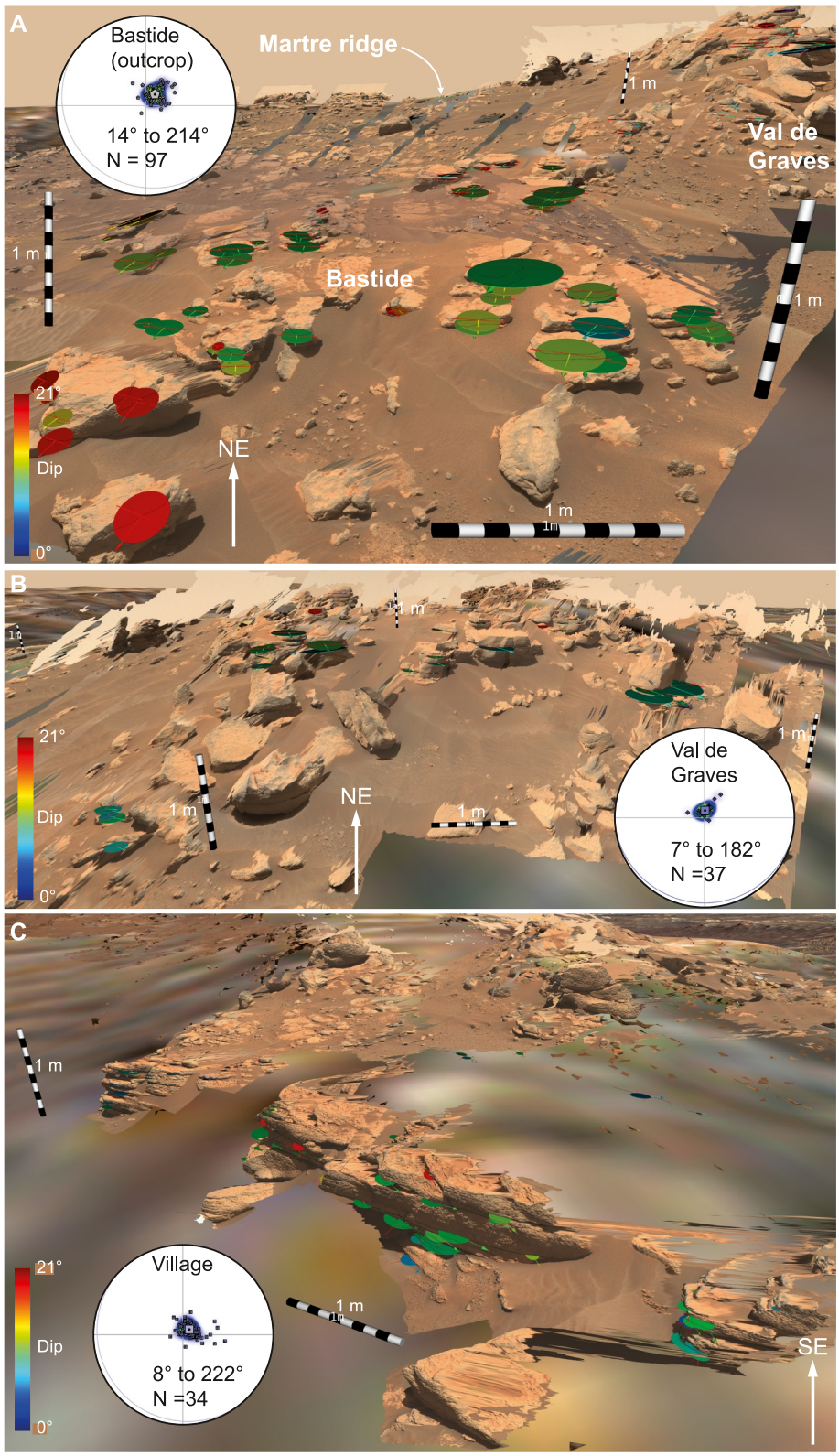

Figure 10. Mastcam-Z OPCs of outcrops in southwest Martre ridge visualized in PRo3D, showing the dips measured from the digital outcrop model as disks colored by dip magnitude. Hemisphere equal area stereonets with layer orientations at each outcrop, plotted as poles to the planes. Scale bars are 1 m. (a) Bastide; (b) Val de Graves; (c) Village –(Credit: NASA/JPL-Caltech/ASU/MSSS/Joanneum Research/VRVis). See Supporting Information S1 for image mosaic details.

10.1029/2025JE009463

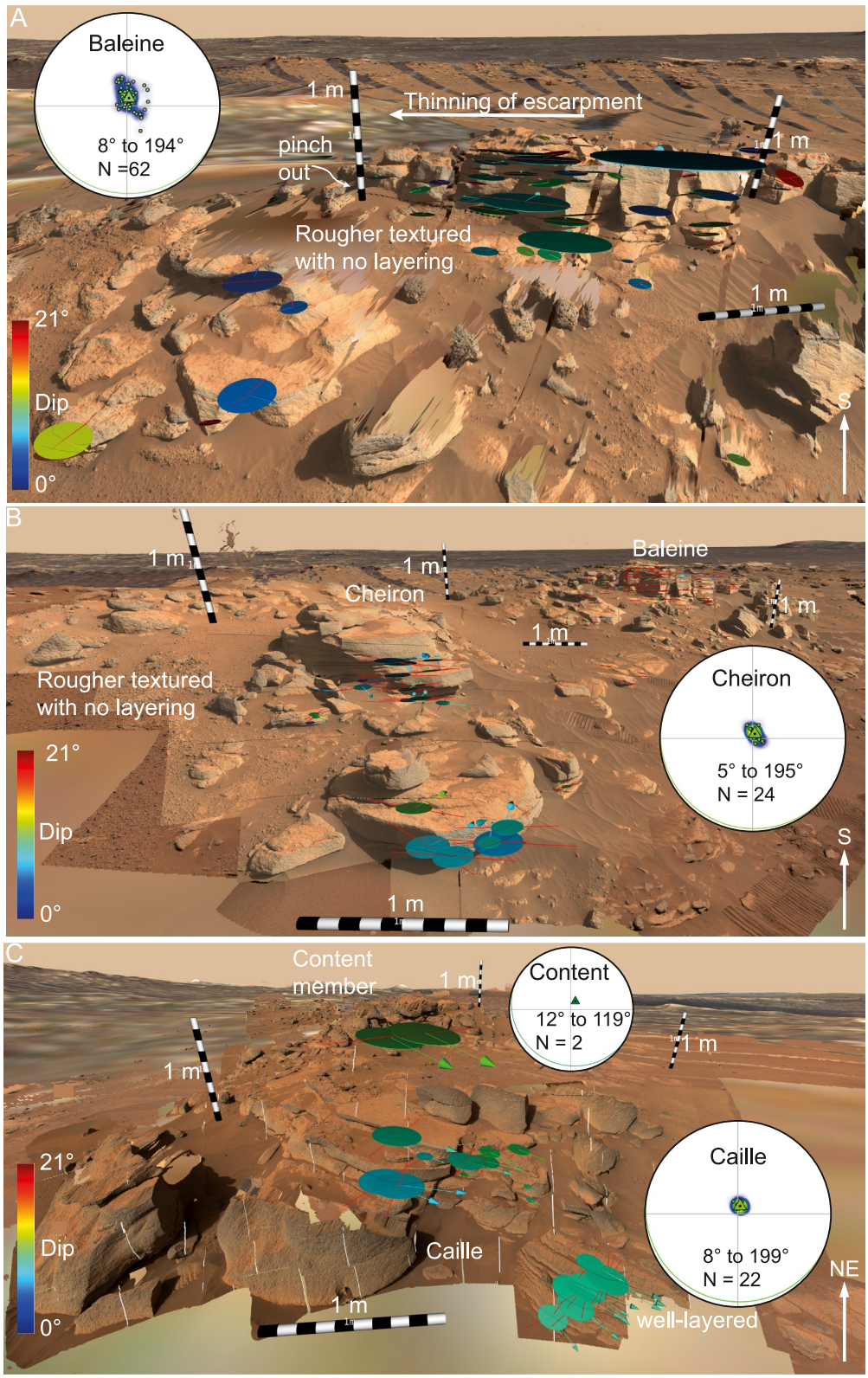

Figure 11. Mastcam-Z OPCs of outcrops in northeast Martre ridge, at the northernmost extent of the south Séítah transect, visualized in PRo3D, showing the dips measured as disks colored according to magnitude, and with inset lower hemisphere equal area stereonets with layer orientations at each outcrop, plotted as poles to the planes. Scale bars are 1 m. (a) Baleine; (b) Cheiron; (c) Caille (Credit: NASA/JPL-Caltech/ASU/UoA/MSSS/Joanneum Research/VRVis). See Supporting Information S1 for image mosaic details.

10.1029/2025JE009463

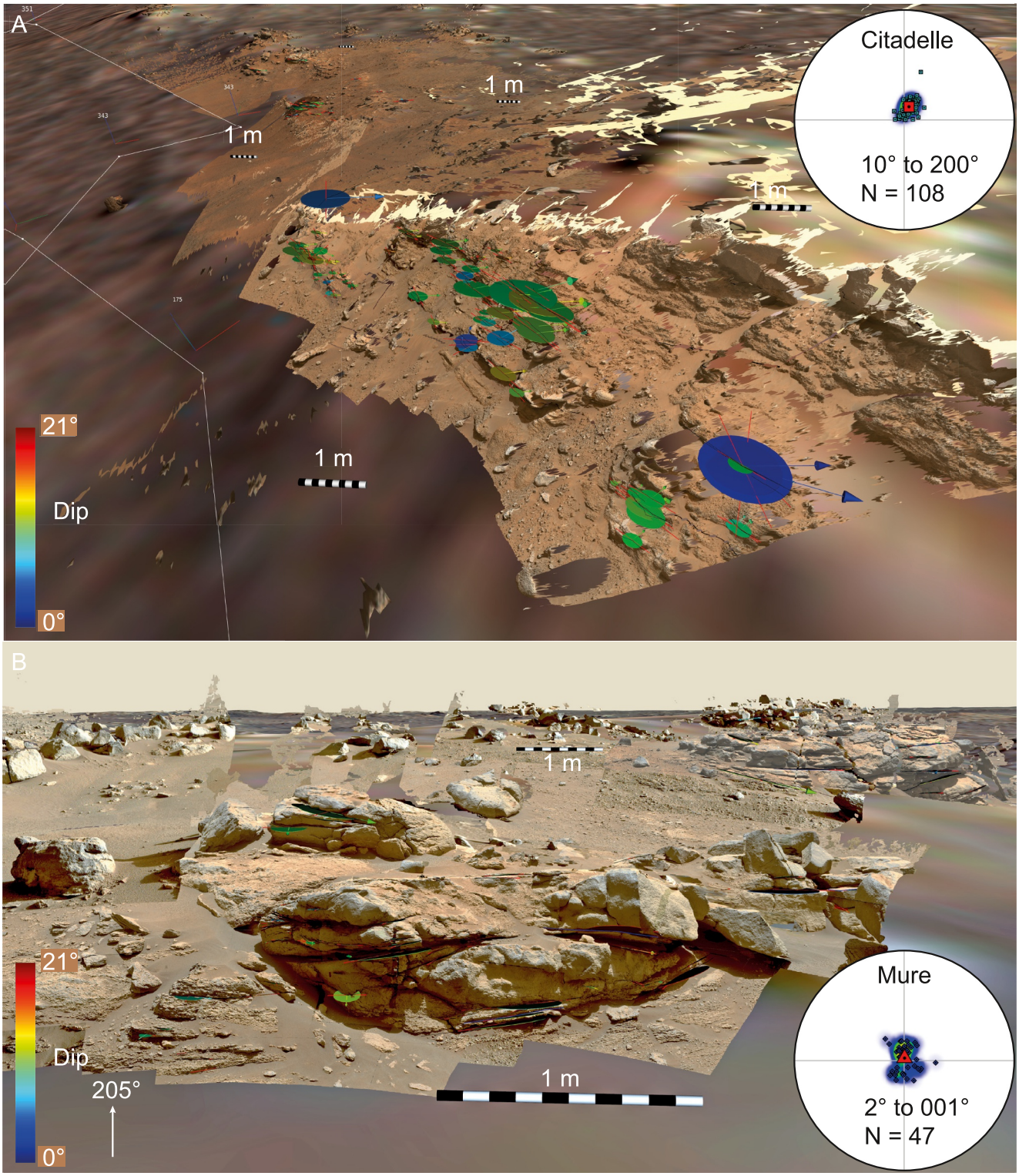

Figure 12. Mastcam-Z OPCs of outcrops in northeast Artuby ridge visualized in PRo3D, showing the dips measured as colored disks and with inset lower hemisphere equal area stereonets with layer orientations at each outcrop, plotted as poles to the planes. Scale bars are 1 m. (a) Artuby; (b) Digital outcrop model of the Mure outcrop showing the variable thickness layering forming discrete, internally structureless lenses of rock that may resemble ancient lava flow structures (Credit: NASA/JPL-Caltech/ASU/UoA/MSSS/Joanneum Research/VRVis). See Supporting Information S1 for image mosaic details.

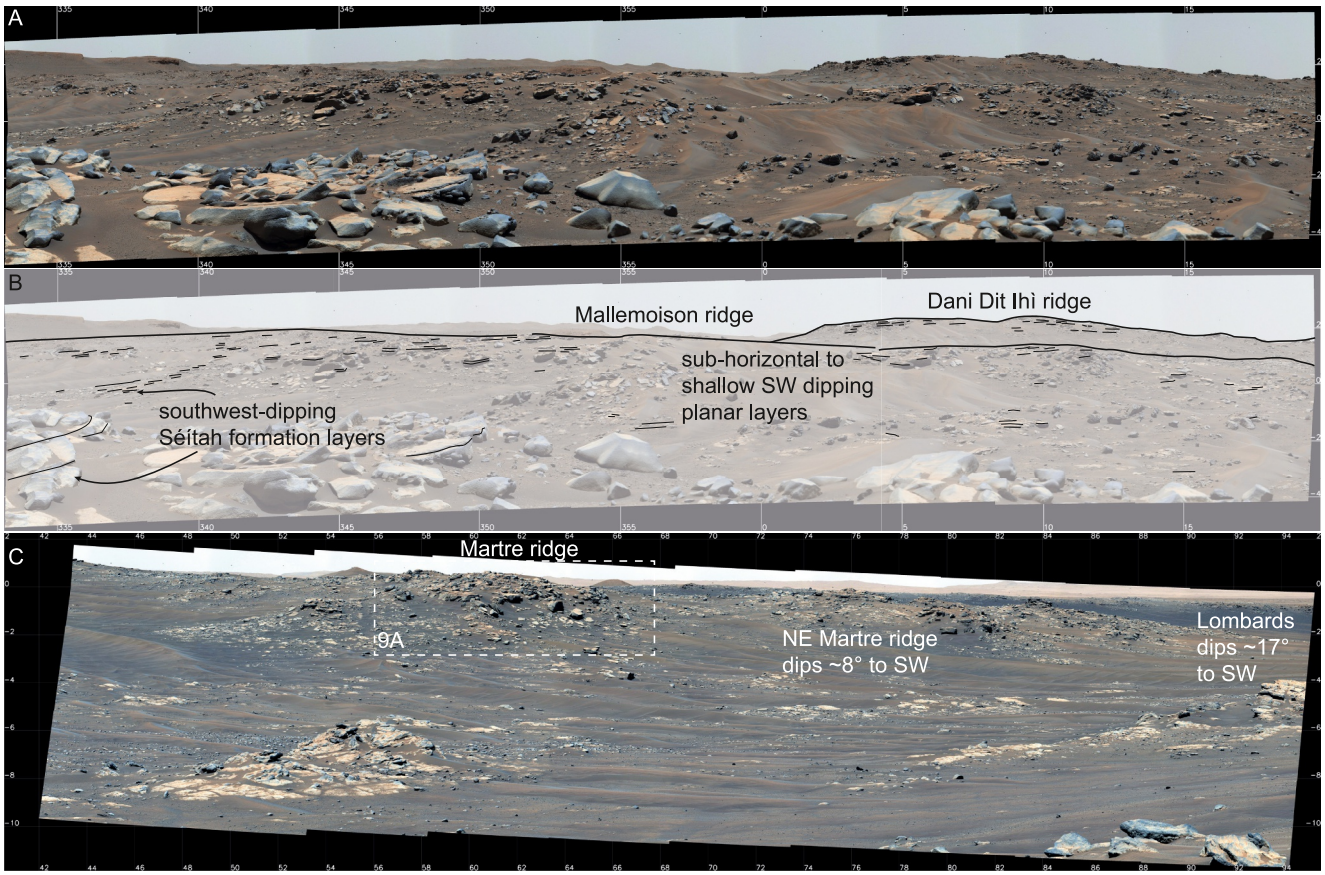

Figure 13. Overview Mastcam-Z panoramas showing the outcrop characteristics of the Séítah formation in outcrop. (a) The Mallemoison, and Dani Dit Ihi ridges veiwed from Artuby Ridge on Sol 201 (zcam08221); (b) Sketch outline of discernible layering in the Mallemoison and Dani Dit Ihi ridges shown in panels (a, c) The Martre ridge viewed on Sol 200 (zcam08216) from the Séítah-Máaz contact region (Credit: NASA/JPL-Caltech/ASU/MSSS).

drive rover location was approximately perpendicular to the Séítah-Máaz boundary here. This radargram does not cross the contact, and whilst the data is noisy, we can observe the base of the Máaz formation at ~6 m depth at the rover's position on Sol 116, together with faint reflectors at the interpreted level of the Séítah formation, which appear to dip to the northeast (Figure 6b).

5.6.3. Northwest Margin of the Séítah Dome

Perseverance acquired little data from the northern margin of the Séítah dome because it was in "Rapid Traverse" mode, driving rapidly to the basal deposits of the Jezero western fan. Thus, our understanding of the northeastern part of Séítah is limited to Mastcam-Z observations from a few sites, a single RIMFAX GPR traverse perpendicular to the Séítah-Máaz contact, and images from the Ingenuity helicopter. The Rapid Traverse exploration mode took *Perseverance* around the northeast bulb of Séítah outcrop past La Orotava and toward the Jezero Western fan front just north of Hahootsa (Figure 2). Parts of the Navcam mosaic collected prior to the RIMFAX scans at La Orotava (Figure 14d) and north of Hahootsa (Figure 14e) show the contact between the Séítah and Máaz formations, but no layer dips can be resolved. The Séítah-Máaz boundary was not crossed on either of these traverses. The longer distance Mastcam-Z mosaics, orbital data and RIMFAX radargrams from these drives are informative in helping us extrapolate our observations from south Séítah. The 3D view in Figure 15a clearly illustrates the topographic relationships outlined in Figure 3, which would be consistent with the structural measurements acquired in south Séítah. The Máaz formation forms flat plains around the rugged Séítah topography, from which the mosaic in Figure 15b was taken, showing a promontory of Séítah rocks ~15 m above the surrounding, yet stratigraphically overlying, Máaz formation plains.

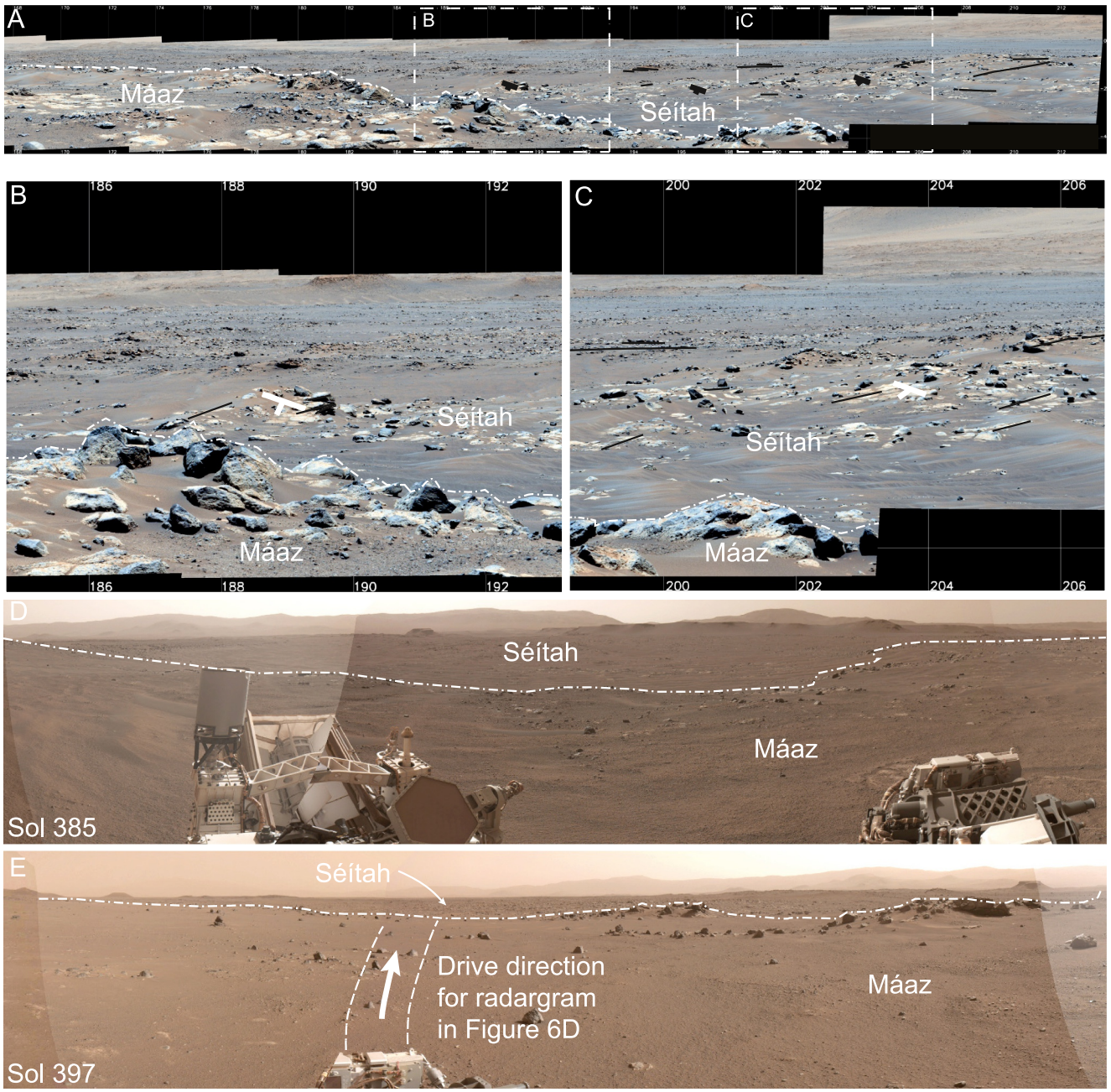

Figure 14. (a) View to the southwest from the northeast margin of south Séítah taken on Sol 117 (zcam08110). Enlarged views of Séítah layer dips are shown in panels (b–d) Navcam view toward the Séítah dome from Sol 385; (e) Navcam view toward the Séítah dome from Sol 397 (Credit: NASA/JPL-Caltech/ASU/MSSS).

5.6.4. Subsurface Data in Northwest Séítah

Radargrams approximately perpendicular to the strike of the Séítah-Máaz contact, were collected in northwest Séítah on sols 385–386, and 398 (Figure 2). Though Mastcam-Z data does not cover the contact in these areas in a lot of detail, it is visible in Navcam images (Figures 14d and 14e) and the RIMFAX GPR data (Figures 6c and 6d). The apparent thickness of the Máaz formation increases away from the Séítah-Máaz contact in the subsurface, and the horizons that define it show a shallow inclination hinting at a not-insignificant apparent dip. This apparent thickening and rotation is interpreted to be further indicative of uplift of the Séítah and Maaz formations together, resulting in the tilted radargram horizons. This interpretation contrasts with a scenario involving uplift and erosion of the Séítah formation followed by emplacement of the Máaz formation, which would be expected to produce

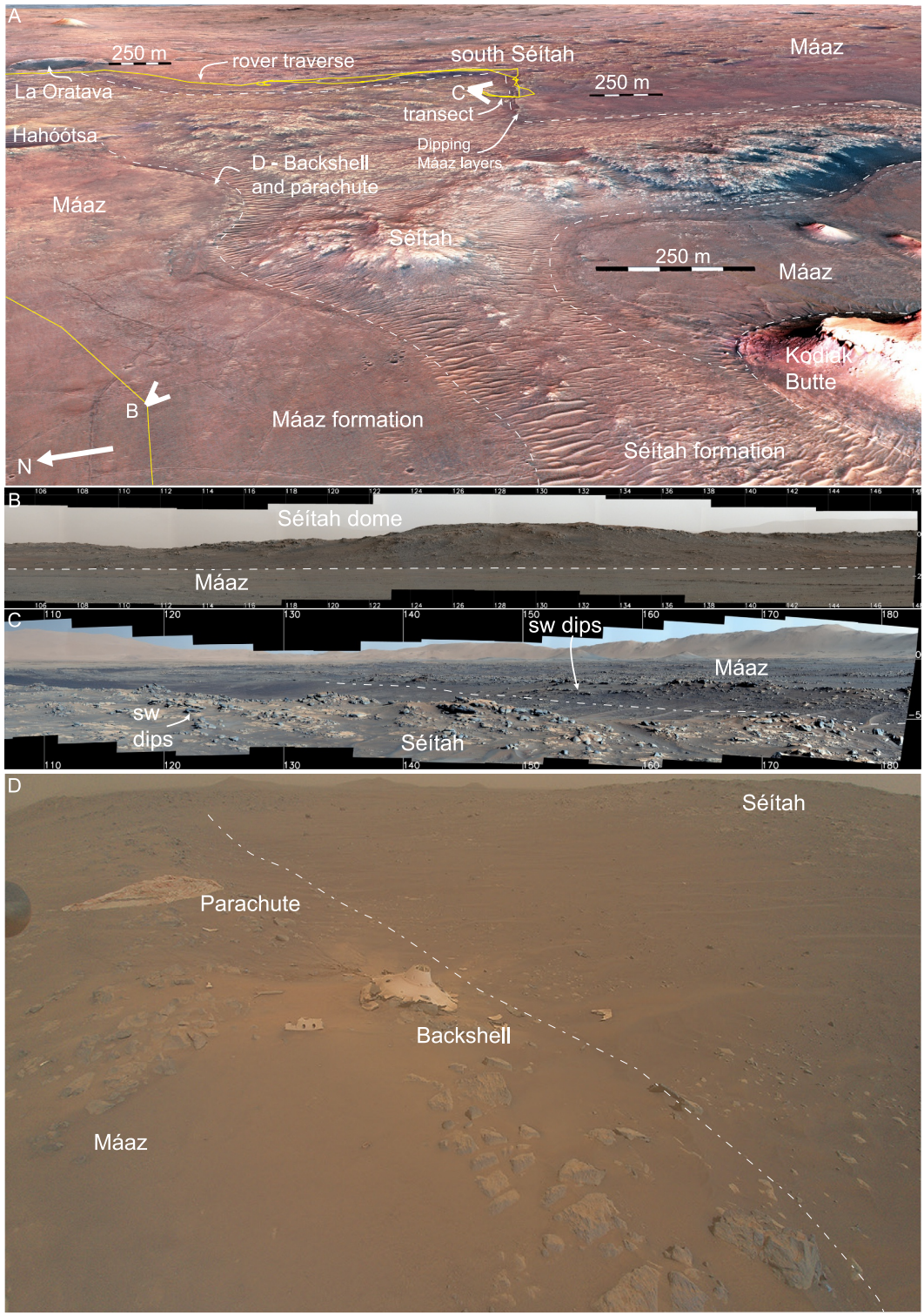

Figure 15. (a) 3D southward looking HiRISE view of the Séítah formation taken from the western fan, showing its general higher topography than the Máaz formation (Credit: NASA/JPL-Caltech/MSSS/UoA); (b) View of high-topography Séítah formation rocks over the adjacent, flat and low-lying Máaz formation in the foreground, taken on Sol 410 (zcam08426, position shown in A); (c) View of Séítah formation layers dipping to the southwest, in the same direction as the overlying Rochette and Artuby members of the Máaz formation. The imaging was carried out on Sol 279 at the position shown in A (zcam08294) (Credit: NASA/JPL-Caltech/ASU/MSSS); (d) Helicopter image of the northwest Séítah-Máaz contact, showing the final location of the EDL system's backshell and parachute, as well as Máaz formation rocks dipping to the north (left in the image). The white dashed line represents the surface trace of the contact with the overlying Séítah formation rocks, which show a higher topographic relief in the image background than that observed in the Máaz formation (Credit: NASA/JPL-Caltech/ASU/UoA/MSSS).

RIMFAX horizons from the Máaz unit that truncate against a subcrop of the Séítah formation that lies at a higher structural elevation.

5.6.5. Ingenuity Imaging of the North Séítah-Máaz Contact in North Séítah

Quite fortuitously, the *Ingenuity* helicopter acquired images of the northwestern contact between Séítah and Máaz. While *Perseverance* was in Rapid Traverse mode to the Jezero delta front, *Ingenuity* flew over south Séítah to image the crash-landing site of the Mars 2020 backshell and descent parachute. The hardware happened to land on the Séítah-Máaz contact on Séítah's west edge (Figure 15d, location in 2). Although the Ingenuity images of the area do not permit construction of a DTM, it appears qualitatively that ridges of the Máaz formation slope down to the northwest, that is, they slope upwards to the southeast toward the outcrops of the Séítah formation rocks.

6. Geological Cross-Section Along the South Séítah Transect

The systematic variation in layer orientation of the Séítah and Máaz formation rocks indicates that the strata of both formations may have been locally deformed. To characterize the geometry of this deformation and to evaluate the subsurface structure, we constructed a cross-section along the south Séítah transect trending 038°–218° from the outcrops of the Máaz formation exposed to the southwest of the Artuby ridge to the Caille outcrop at the northeastern extent of the Martre ridge (Figure 16a). This line of section is sub-parallel to the trend of the south Séítah transect (Figure 4), and to the mean dip directions measured at the outcrops along the traverse. This enables us to build a representative picture of the structural geometry of the exposed stratigraphy. Figure 16a shows the location of the key outcrops analyzed using Mastcam-Z OPCs, together with stereonets summarizing the dip and strike values extracted from exposed layer contacts at each location. Some outcrops were grouped together for cross-section construction (inset Figure 16a), due to their proximity and relative uniformity of dip and geometry in outcrop. The relative locations of the outcrops were plotted on the topographic profile in Figure 16b together with the mapped stratigraphic boundaries. We calculated the mean layer orientations at each location and used these data to define domains of roughly equal dip along the lines of section. The planes described by the mean vectors at each location were used to define four distinct dip domains stretching from NE-SW. We used the kink-band cross-section method to correlate and reconstruct the cross-sectional geometry based on the assumption of constant thickness, where bisecting axial traces are used to ensure that the layer thickness remains constant across dip domain boundaries.

6.1. Identification of Dip Domains

We identified four distinct dip domains in the south Séítah transect, presented here from the northeast to southwest ends of the south Séítah transect (Figures 16a and 16b). Dip domain 1 covers the area of the section comprised of the Caille, Cheiron, Baleine, Val de Graves and Village outcrops at the northeastern end of the transect. The stereonet of combined values from the Caille-Baleine outcrops yields a mean plane dipping 6° toward 199°, and the stereonet for Val de Graves and Village yields a plane 7° dipping toward 221° (Figure 16a). The dip azimuth of the Caille-Baleine data is approximately 20° oblique to the line of section; however, this only reduces the apparent dip by 1° and was not deemed sufficient to create an additional dip domain.

Dip Domain 2 (Figure 16b) comprises the area containing the Bastide outcrop and exposures of the Séítah formation ∼50 m to the west of the line of section. Average dips of 13° toward 217° and 11° toward 219°, respectively, were collected from these outcrops (Figure 16a). Dip domain 3 was constructed from dips collected at the Issole, Lombards and Artuby ridge outcrops, where the dip increased to an average ∼16° at the boundary between the Séítah and Máaz formations. Individual layer dips at the Lombards and Issole outcrops were more variable than those measured elsewhere in the Séítah formation, partly due to poor preservation of layer contacts and 3D artifacts caused by large imaging distances. The average plane orientation at Lombards and Issole was 16°–207° and 15°–216° at the Artuby ridge. These are similar enough to be considered identical and are thus combined to form a third dip domain.

Dip domain 4 is defined from images of Máaz formation exposures southwest of the Artuby ridge, which were collected prior to the commencement of the transect on Sol 184 (Figure 7a). Here, Mastcam-Z image mosaics show that layer dips are nearly horizontal. No quantitative 3D data were obtained at this location. We have projected the estimates of the Máaz surface dips to depth to define dip domain 4 and placed the bounding axial

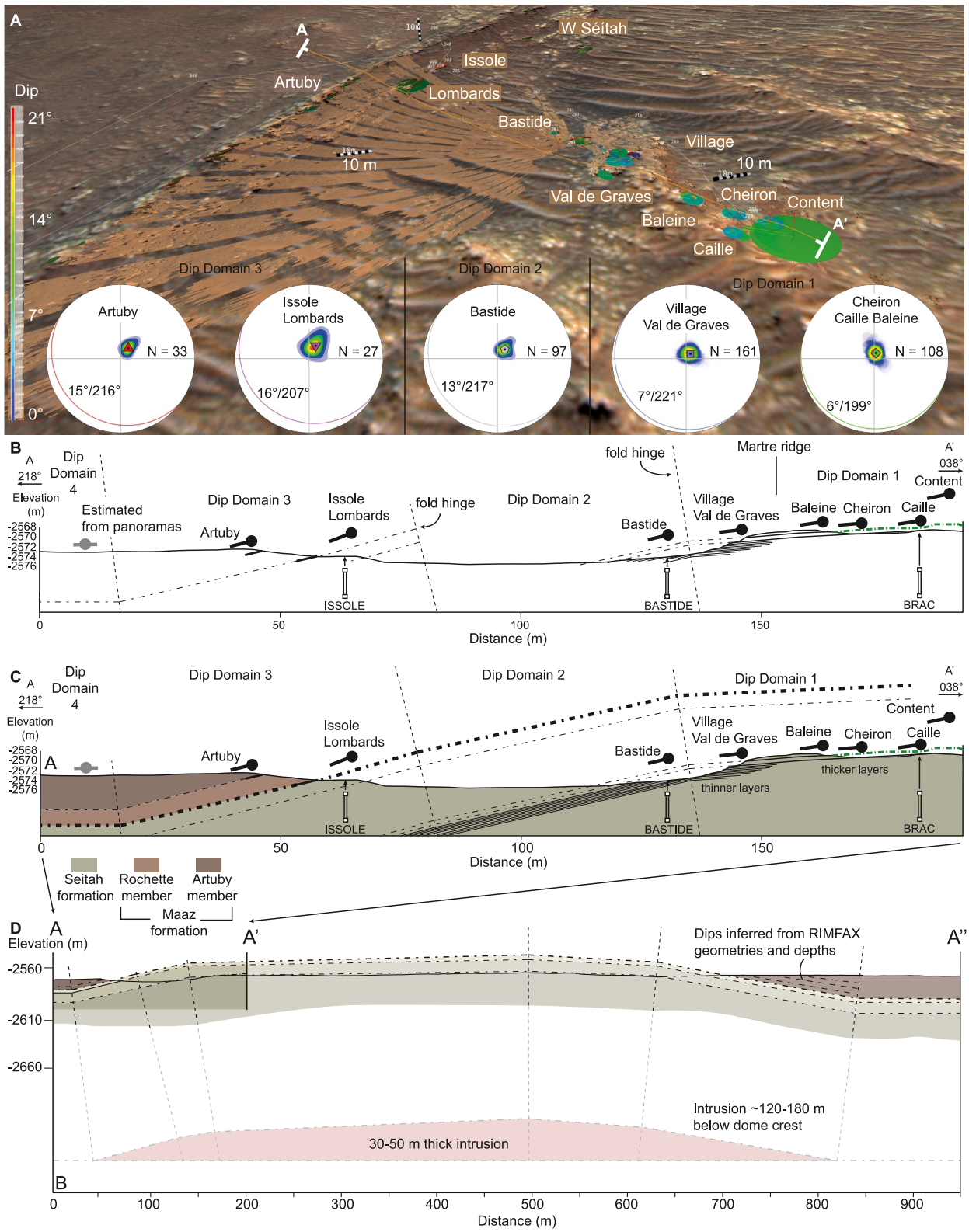

Figure 16.

trace just to the northeast of the position at which the dipping surface layers in the Máaz are either horizontal or buried by regolith.

6.2. Cross-Section

The defined dip domains are shown in a cross-section along the south Séítah transect in Figure 16b, with additional interpretation shown in Figure 16c. This cross-section provides a reference framework for relating the stratigraphic position of the observed lithologies. We interpret the thinly layered lithology observed at the base of Caille, and at the Village and Bastide outcrops as the stratigraphically lowest strata observed in the south Séítah transect. The different dip domains (1–4) are the basis for the extrapolation of our observations above and below the present-day ground surface. Dip measurements indicate that the rocks are young to the southwest if we maintain the assumption that the rocks are the right way up; therefore, rocks at Lombards and Issole are younger than those exposed at the Martre ridge. As shown in the cross-section in Figure 16c, the up-dip projection of the base of the Lombards outcrop, assuming constant thickness, places it at approximately 13.5 m, stratigraphically above the upper boundary of the thinly bedded Bastide member rocks exposed at Caille, Village and Bastide.

The cross-section shows that layer dips increase from northeast to southwest approaching and just beyond the Artuby ridge, and then decrease to near horizontal in the Máaz formation exposures southwest of the Artuby ridge. At the northeastern end of the section, on the Martre ridge, layering is sub-horizontal with dips consistently measured at ∼5°–6° to the south. We observe a ∼7° increase in dip toward the southwest between the Val de Graves and Bastide areas. The layers are seen to dip consistently between 11° and 13° toward ∼218° from Bastide to the southwest. We measured an increase in overall dip to ∼16° toward 207° in outcrops of the Séítah formation at Lombards and Issole, at the base of the Artuby ridge. Similar dips (∼15°–216°) were measured on layers on the Artuby ridge above the Séítah-Máaz formation boundary. This leads us to infer that the Séítah and Máaz were deformed together after the emplacement of the Máaz basalts. These changes in geometry, together with the flattening out of the Máaz formation to the southwest, can be extrapolated and correlated in the cross-section to describe a sigmoidal layer profile form, with the Séítah-Máaz boundary flattening out at a depth of ∼16 m below the present-day topographic surface. The steepest part of the profile indicated by the dips from Bastide to Artuby ridge (dip domains 2 and 3) can be extrapolated above the present-day surface to intersect the axial trace bounding dip domains 1 and 2. The sub-horizontal layering at the Martre ridge completes the sigmoidal morphology. There is no evidence in images to indicate any significant change in dip northeastwards of the end of the south Séítah transect, and views toward central Séítah show predominantly sub-horizontal dips in layering exposed in the ridges there (Figure 13).

6.3. Extending the Geological Cross-Section Across the South Séítah Dome

The south Séítah transect (Figure 16c) covers only ∼20% of the exposed south Séítah inlier (Figure 1). We extrapolated the cross-section northeastwards across the entire width of south Séítah to characterize the full geometry of the structure. We estimated bedding geometries in the central region of south Séítah using long distance Mastcam-Z and SuperCam RMI images, and data collected at the northeastern boundary between the Séítah and the Máaz formation during the rover traverse around the edge of the south Séítah outcrop. Figure 16d shows an extrapolated cross-section. In the central part of the south Séítah inlier, long distance surface observations show that topographic high points in the landscape, such as at the Dani Dit Ihi ridge, are formed by the upper massive blocky unit with sub-horizontal layering (Figure 13). Evidence for steeper dipping bedding, such as that observed at Artuby ridge and Citadelle, is absent northeast of the transect.

At the northeastern margin of South Séítah, the rover did not traverse into the Séítah formation outcrop area, but RIMFAX radargrams show northeast dipping subsurface reflectors ∼6 m beneath gently inclined Máaz formation

Figure 16. (a) 3D view of the HiRISE orbital image and topography data merged with Mastcam-Z OPCs along the South Séítah transect traverse. The orange line indicates the location of the line of cross-section A-A'. Insets are the equal area stereonets showing the mean vector pole on top of contours delineating the spread of values. The stereonets show the vector means of the combined data for the key outcrops that were used to define the dip domains. A gradual increase in average dip is observed from Caille in the NE to Artuby ridge in the SW. (Credit: NASA/JPL-Caltech/ASU/MSSS/Joanneum Research/VRVis); (b) Topographic profile A-A′ with averaged dips and outcrop locations projected onto the profile. Dip domains were defined for fold hinge placement. The location and inferred dip of fold hinges that bound the dip domains are shown as black dashed lines. Sample locations are shown: (c) Cross-section A-A′ through the south Séítah transect; (d) Extension of cross-section A-A′ to A" to speculate on the geometry of south Séítah and the proposed formative intrusion as a whole. See Figure 1b for section location.

(Roubion member) rocks; these are inferred to come from Séítah formation rocks (Figure 14a). We measured dips of ∼10° to the northeast based on outcrop patterns and RIMFAX subsurface geometries (Figures 6b); 6 m depth at the distance at which the radargrams were collected from the Séítah -Máaz contact (Figure 6a) is consistent with a 10° dip. We projected the Séítah-Máaz boundary along the line of section to intersect with the northeast boundary, maintaining the kink-band constant thickness model. Regional elevation in the cross-section is ∼6.5 m higher in the northeast than in the southwest, but the dips in the southwestern region are not obtained from on-the-ground stereo-data, so there is some uncertainty.

7. Discussion

7.1. Structural Analysis of the South Séítah Dome

This study examines the geometry of the Séítah dome and its relationship to the Máaz formation using structural data from the south Séítah transect across the Séítah–Máaz transition. The observed structural variation is consistent and systematic, allowing us to constrain the deformation style and infer the mechanism. Any model for the structural geometry and emplacement mechanism of the Séítah formation requires explanation of the following observations in south Séítah:

1. Séítah formation rocks show a progressive increase in bedding dips from the NE extent of the transect (within the interior of Séítah) toward the Artuby ridge, close to the Máaz- Séítah boundary. Dips flatten out abruptly to the southwest of the Artuby ridge. t
2. The Rochette and Artuby members of the Máaz formation exposed on the Artuby ridge show similar bedding dips of 14–20° toward 205°–215° as seen in the underlying beds of the Séítah formation at Issole and Lombards.
3. Dips are sub-horizontal southwest of the Artuby ridge close to the Séítah-Máaz boundary.
4. Exposures of the Séítah formation within the main part of the South Séítah inlier lie at a higher elevation than rocks of the Máaz formation on either side of the inlier.
5. Layering in the Bastide member of the Séítah formation in the central part of south Séítah is sub-horizontal and does not show the steeper inclinations observed at the boundary with the Máaz formation at the Artuby ridge.
6. Ground penetrating radar data from RIMFAX at the NE flank of south Séítah indicate that Séítah formation rocks in the subsurface dip to the NE away from south Séítah. Layer dips on the opposing SW flank of south Séítah at the Artuby ridge dip in the opposite direction, as observed at the surface and in RIMFAX data.
7. Ingenuity images from near the northwest boundary of South Séítah show layering that dips northwest, away from South Séítah.

7.2. Folding Explains the Structural Geometry of the South Séítah Inlier

The cross-section constructed along the south Séítah transect (Figure 16c) leads us to interpret the variation in bedding dip as the result of deformation by folding of lithified layers of the Séítah formation and overlying Máaz formation. Specifically, the layer geometry observed in south Séítah forms a monoclinal fold. Extrapolation of the cross-section northeastwards into the center of the inlier and to its NE-margins (Figures 13–15), and comparison with image and GPR data in the northwesterly regions, shows that this relationship is consistent around Séítah. These observations lead us to interpret the overall structure of south Séítah as a gentle, upright, composite quaquaversal dome with a broad crest comprised of sub-horizontal layers and surrounded by fold limbs dipping away from the crest that have undergone significant post-fold tilting. The highest uplift in the structure is expected in the central part of the present day Séítah dome outcrop, which also coincides with the highest topographic relief in the area (Figure 3). Deformation appears to be focused at the edge of the Séítah formation outcrop, with the overall structure forming a low amplitude flat-crested box-shaped fold. The abrupt decrease in bedding dips away from the edge of the Séítah formation outcrop at the Artuby ridge is clear evidence of the localized nature of deformation. One caveat is that the outcrops southwest of the Artuby ridge have been interpreted as later-emplaced Máaz formation units, possibly emplaced concurrently with, or subsequent to, the uplift (Crumpler et al., 2023; Thackston et al., 2024). This would add uncertainty to the southwestern part of the cross-section in Figure 16d, where extrapolation of surface observations to depth would not yield a true image of the dome geometry. Radargrams collected by the RIMFAX instrument directly over the Séítah-Máaz contact however (Figure 6a, radargram location in Figure 4), do support a constant thickness assumption in this area, implying parallel emplacement.

We estimate ~30–50 m of maximum fold crestal relief over a transect distance of ~165 m based on observations of surface dips, surface morphology, and subsurface inferences from RIMFAX radargrams (Figure 16). We plotted a great circle of best fit through the mean values of dip and strike measured at key outcrop locations to constrain the fold axial trace trend and plunge. At the south Séítah transect, the fold axis trends 124°–304° and is horizontal, indicating an upright fold geometry (McClay, 1987) and therefore not modified after folding.

In addition to dip variations across the fold limbs, we observed a systematic decrease in deformation intensity along the strike. At the Artuby ridge outcrop at the southwestern end of the south Séítah transect, beds of both the Séítah and lower Máaz formations dip 14–20° to the SW, defining the steepest limb geometry. In contrast, at Citadelle (Figure 2), dips average 10° to the southwest, and ~250 m southeast of Artuby, the bedding dips at Mure flatten to 2°. This along-strike gradient in limb dip, and therefore crestal uplift, suggests non-cylindrical fold geometry, consistent with a slightly southeast-plunging antiformal structure. Such tapering of amplitude and limb dip along strike is typical of forced folds above laterally restricted intrusions, where inflation is localized and wanes outward.

7.3. Relative Timing of Deformation

At the southwestern part of the south Séítah transect, it is clear that Séítah rocks lie beneath the Artuby and Rochette members of the Máaz formation. Layering in these Séítah rocks (Issole and Lombards outcrops) is concordant with layering in the overlying Máaz rocks exposed on the ridge. We infer that the Séítah formation and lower Máaz members at south Séítah were emplaced paraconformably (separated by a sub-horizontal bounding surface) and tilted together. This suggests that at least the lower members of the Máaz formation once extended across the erosional windows that currently expose Séítah formation rocks, prior to uplift in the Séítah dome.

7.4. Folding Explains Topographic-Stratigraphic Relations of Crater Floor Units

Even before *Perseverance*'s landing, it was puzzling to observe that outcrops of the Séítah formation, exposed in apparent erosional windows, stood at higher elevations than the flat lying Máaz rocks surrounding the window. In south Séítah, the highest exposures of Séítah formation rocks are at least 17 m above the adjacent (and stratigraphically higher) Máaz formation rocks (e.g., Figures 3 and 15). This apparent anomaly suggested that the whole section was deformed by localized uplift and related folding.

7.5. What Caused the Deformation of the Séítah Formation in the Séítah Inlier

We interpret the deformation of crater-floor units at south Séítah as the result of localized folding of these igneous layers. The cause of the deformation has not been constrained so far (Farley et al., 2022). Here we consider the plausible mechanisms for doming and folding and develop a model for intrusion-related deformation. Folding of rocks is ubiquitous in tectonically deformed terrains on Earth, commonly occurring to accommodate movement above low-angle (<40°) contractional thrust faults (Bilotti & Shaw, 2005; Briggs et al., 2006; Corredor et al., 2005; Erslev, 1991; Jolly et al., 2016; Suppe, 1983; Suppe et al., 1992; Suppe & Medwedeff, 1990), or above weak decoupling or detachment layers (Buxtdorf, 1916; Casciello et al., 2009; Epard & Groshong Jr, 1993; Homza & Wallace, 1995; Mitra, 2003; Poblet & McClay, 1996). Folding has also been documented to occur as a response to deformation ahead of extensional faults (Hardy & McClay, 1999; Sharp et al., 2000), to accommodate slip on high-angle (>40°) blind faults formed due to contractional (Braathen et al., 2020; Cosgrove & Ameen, 1999; Sattarzadeh et al., 1999; Stearns, 1978; Yonkee & Weil, 2015), extensional (Lewis et al., 2015; Withjack et al., 1990) or shearing strain (Harding et al., 1985) or differential compaction (Cosgrove & Hillier, 1999) acting on a layered series of rocks.

Folding also naturally accompanies impact crater formation, both during the early and later stages of crater formation (e.g., Kenkmann et al., 2013, 2014). Some folding relating to for example, thrusting, normal faulting, and formation of tight isoclinal folds (Kenkmann, 2002) are well-known in both impact craters and other geologic environments, while others, such as folding relating to formation of central ring moats and radial transpression ridges (Kenkmann & von Dalwigk, 2000), may be more distinctive for the impact environment (when mapped in full context). At Jezero crater, rocks and structures relating to the crater floor or any central uplifted feature (if ever present), are believed to be hidden underneath significant amounts of post-impact deposits (Ehlmann et al., 2008; Schon et al., 2012). This means that structural features observed on the floor of present-day Jezero

crater are unlikely to be related to crater formation (although later processes may have re-activated impact-related structures).

There is no evidence that the dome of south Séítah was formed by regional-scale tectonic deformation, nor by impact cratering, or serpentinite diapirism. There is little evidence for tectonic deformation in the Jezero area in general. Although lithospheric bulging due to Tharsis emplacement may cause regional scale deformation (Sholes et al., 2021), this is expected at a far larger scale than the folding observed at Séítah. The Jezero crater itself is circular and not foreshortened or elongated by obvious fault systems, which may have been suggestive of post-impact tectonic modification (Figure 1). Nor do any of the extensional grabens of Nili Planum cross into Jezero; they are all to the north and west, so it is unlikely that the crater has undergone considerable extensional deformation. The isolated broad-crested rounded and multi-lobate geometry of the fold is not consistent with a thin-skinned folding style and the dome lacks the vergence and associated faulting that would be expected from thick-skinned deformation such as reactivation of deep-seated basement faults. The multi-lobate planform morphology of Séítah would require deep-seated faults of multiple orientations intersecting at high angles—features absent elsewhere on the crater floor. No folds with north–south trending axial traces or other indicators of such tectonism that could be linked to the observations at Séítah are present. The Séítah dome structural geometry does not show features that would suggest deformation by impact processes. Impact craters, like Jezero, can produce fractures and faults in the surrounding rocks, which can conceivably be activated by later tectonic stresses. However, such faults and fractures are typically concentric and radial to the crater's center, which is not consistent with the multilobate planform morphology of south Séítah (Figures 1 and 3). We discount doming caused by subsurface serpentinization (e.g., Evans et al., 2021; Germanovich et al., 2012) as speculative; only slight serpentinization was observed in olivines in abrasions in the Maaz formation (Tosca et al., 2025) and there is insufficient additional evidence for serpentinite diapirism to be a reasonable mechanism to induce the observed uplift and folding.

7.6. Forced Folding Induced by Igneous Intrusion

We infer that the folding mechanism of Séítah to be a forced fold produced by the emplacement of a shallow intrusion. Intrusion related forced-folding is a well-studied phenomenon on Earth, but this is the first time it has been described from ground-based data on Mars. On Earth, shallow sills and laccoliths commonly generate flat-topped or dome-like broadly symmetrical folds through elastic bending of the overburden (Jackson et al., 2013; Reeves et al., 2018), which form structural and topographic highs (Hunt, 1953; Johnson & Pollard, 1973; van Wyk de Vries et al., 2014). The Séítah dome's flat crest and sharply localized limbs are key features of intrusion-induced forced folding of a thin elastic roof. Plate-bending theory predicts doubly hinged fold geometries with edge-focused bending and failure, and a sill to laccolith transition when the lateral spread reaches ~three times the effective overburden thickness (Pollard & Johnson, 1973), a process that has been well-documented in natural examples on Earth.

Terrestrial examples have been extensively analyzed in both field and sub-surface seismic reflection data sets. Field examples of geometries comparable to Séítah and Gaspe have been documented in well-studied laccolith provinces on Earth, such as the Henry Mountains of Utah (Hunt, 1953), the Spanish Peaks in Colorado (Johnson, 1968), and Torres del Paine in Patagonia (Michel et al., 2008), where flat-topped domes transition sharply into steeply dipping fold limbs above intrusion margins. In these systems, roof deformation is expressed in broad domes bounded by narrow hinge zones, and in some cases is accompanied by radial and concentric extensional faults and fracture sets interpreted to result from outer-arc extensional stresses caused by bending during inflation (Corry, 1988; Magee, 2024; Magee et al., 2017; Michel et al., 2008). Exposures in these provinces also show multi-lobate intrusion roofs and variations in fold amplitude along strike, demonstrating the spatial complexity that can arise from even relatively simple magma pulses.

In offshore settings, extensive examples occur offshore NW Australia, offshore NW Africa and the North Atlantic Igneous Province (NAIP), including the Faroe–Shetland, Rockall and Vøring basins, where intrusion of saucer-shaped sills has uplifted the overburden to produce kilometer-scale, flat-crested forced folds with associated crestal grabens and rim-fault systems (Hansen et al., 2008; Jackson et al., 2013; Kumar et al., 2022; Magee et al., 2017; Omosanya et al., 2017; Planke et al., 2005; Schofield et al., 2012). Folds commonly exhibit low-amplitude, broad central plateaus surrounded by sharp hinge lines, and their associated fault patterns record extensional failure of the roof during peak inflation (Magee et al., 2014). Analysis of three-dimensional seismic

reflection data sets has shown strain from intrusion inflation to produce bending, fracturing, and sometimes faulting of overlying layers focused at the edge of the intrusion (Hansen & Cartwright, 2006; Johnson & Pollard, 1973; Jackson et al., 2013; Kumar et al., 2022; Magee et al., 2017, 2019; Magee, 2024; Reeves et al., 2018; Reynolds et al., 2022). Additional saucer-shaped sill studies highlight diagnostic features such as concentric rim synclines, segmented or lobate sill edges, and marginal faulting that reflect episodic intrusion growth and stress redistribution during inflation. In the Vøring and Faroe–Shetland basins, for example, rim synclines up to several kilometres wide form where the intrusion periphery causes downward bending of the overburden (Planke et al., 2005), while radial segment boundaries mark zones where sill lobes coalesced (Magee et al., 2014; Polteau et al., 2008; Schofield et al., 2010). The absence of such features in Séítah could indicate a more symmetric inflation history, a roof mechanical structure that suppressed peripheral subsidence, or subsequent modification that obscured original rim-zone deformation, or any surrounding synforms that could be infilled. These terrestrial examples of forced folds above sills and laccoliths share key features with Séítah: domal uplifts with broad, mostly flat crests, relatively steep limbs and no consistent vergence, providing some morphological confirmation of a sill or laccolith underlying the Séítah formation outcrop on the Jezero crater floor.

Field evidence from laccolith provinces shows that variations in roof competence and elastic thickness can locally modify hinge positions and fold symmetry. In the Henry Mountains, for instance, roof segments underlain by thicker, stronger sandstone beds display broader crests and gentler limbs, whereas thinner, more compliant roof segments deform into narrow, high-amplitude domes (Gudmundsson, 2011; Hunt, 1953; Johnson & Pollard, 1973). The overburden that was uplifted and folded then eroded to form the present day Séítah and Gaspé outcrops comprises ultramafic and mafic rocks that exhibit layering and therefore anisotropy at the surface. Despite these uncertainties, the constant thickness kink-band technique applied here therefore represents an average condition for the Séítah fold, with local departures from the idealized geometry possible depending on roof-rock heterogeneity.

Multi-pulse inflation could explain the uniform crest dips and along-strike variations in limb dip with each episode incrementally adding uplift in the central areas and rotating fold limbs or reactivating marginal fractures. Comparable overprints of successive intrusion lobes on fold geometry have been reported from both field and seismic studies (Agirrezabala, 2015; Lino & Vlach, 2021; Reeves et al., 2018; Reynolds et al., 2022). In several NAIP and South Atlantic examples, growth of laterally offset sill lobes causes along-strike plunge variations, asymmetry between opposing limbs, and even hinge migration over distances of hundreds of meters (Galland et al., 2019, 2022; Magee et al., 2014; Spacapan et al., 2017). In Patagonia, multiple emplacement pulses into the same roof produced local steepening of previously gentle limbs (Leuthold et al., 2012, 2013; Michel et al., 2008), while in seismic data from the Santos Basin, Brazil, multi-lobate sills generated complex fold interference patterns where they interact with salt deposits (Magee et al., 2021). These examples illustrate that the plunging fold hinges and subtle along-strike variations at Séítah could plausibly arise from staggered inflation episodes.

7.7. How do the Dimensions of the Séítah Dome Compare to Terrestrial Intrusion-Induced Forced Folds?

Fold relief and length can be used to approximate intrusion dimensions (Hansen & Cartwright, 2006), although this relationship is modified by strain accommodation style (Jackson et al., 2013). The scaling relationships between intrusion thickness or fold amplitude and intrusion/fold length are well established in both natural and experimental settings (Magee et al., 2017; Magee, 2024 and references therein). In purely elastic flexure, fold geometry reflects the shape and uplift of the intrusion, host-rock strength, anisotropy, and uplift angle (Stearns, 1978). The magnitude and distribution of roof deformation also depend on factors such as the effective elastic thickness of the overburden, the presence of mechanically contrasting layers, and the onset of inelastic failure once bending stresses exceed rock strength (Bunger & Cruden, 2011; Galland et al., 2014; Gudmundsson, 2011; Menand, 2011). For example, layered roofs with weak shale or tuff horizons tend to concentrate deformation into narrow hinge zones (Hudleston & Treagus, 2010; Johnson & Pollard, 1973; Ramsay, 1967), producing higher local limb dips than homogeneous roofs of similar thickness. Such controls can both mimic and obscure purely geometric scaling relationships (Fletcher, 1991; Ramsay & Huber, 1987), and they offer a possible explanation for the relatively uniform dips observed in the Séítah fold despite its considerable inferred diameter.

Experimental and field data (Kumar et al., 2022; Magee et al., 2017; Montanari et al., 2017) show that inelastic processes (host-rock compaction, pore-fluid expulsion, and faulting) decouple relief from intrusion thickness and therefore reduce amplitude/thickness ratios between the fold and intrusion, meaning observed relief

underestimates true intrusion thickness. We see no evidence for faulting, collapse, or fluidization at Séítah, and the igneous textures of crater-floor rocks suggest limited compaction. The fold amplitude and width therefore provide a minimum approximation of intrusion size: ∼1 km diameter and up to 50 m thick, based on two-dimensional geometry at the south Séítah transect. The measured crestal uplift of 47 m in Figure 16d likely increases northwest and decreases southeast, and the crestal length-to-uplift ratio of 21.3 matches published laccolith dimensions (Magee, 2024).

Scaling relations (Hansen & Cartwright, 2006; Jackson et al., 2013; Magee, 2024; Magee et al., 2013, 2017; Morgan et al., 2008) indicate that laccoliths typically have length-to-uplift (L/A) ratios of ∼10–25, saucer-shaped sills up to ∼30 (Hansen & Cartwright, 2006); similar values are reported in sedimentary basins and as low as 8 in layered magmatic provinces (Spacapan et al., 2017). At Séítah, the ∼1 km fold width and ∼30–50 m relief yield an L/A ratio (∼20–33) within the terrestrial range for small laccoliths and thick sills (Hansen & Cartwright, 2006; Magee, 2024; Poppe et al., 2024), supporting a shallow-emplacement origin. Our L/A ratio for Seitah of ≈20–33 lies squarely in the elastic regime for shallow intrusions predicted by elastic-plate gravity-current theory for terrestrial laccolith thickness–length relations (Michaut, 2011), and elastic growth models that include magma body forces and fracture-controlled propagation, yielding flat-topped, steep-sided geometries with L/A ∼10–30 (Bunger & Cruden, 2011). In seismic data sets, fold amplitude commonly underestimates sill thickness because inelastic processes (compaction, minor faulting) and late deflation partially decouple uplift from net intrusion thickness; thus, our 30–50 m crestal relief is a lower bound on the causative intrusion thickness.

Figure 17 presents a compilation of length-amplitude scaling relationships for terrestrial and experimental data, including forced folds above sills and laccoliths, as well as intrusion thicknesses derived from seismic studies of mafic and felsic intrusions. Individual data sets are grouped by intrusion type and source.

Overlain on the scatterplot in Figure 17 are two shaded regions corresponding to the Gaspé and Séítah dome structures (Figure 3). The thickness of the postulated sub-Seitah intrusion is unknown, but we use the mapped fold amplitude to approximate this thickness. The Séítah topographic range (green) spans a fold length of approximately 800–1,200 m and an uplift of 58–66 m, based on the maximum outcrop elevation relative to the surrounding Máaz formation. The cross-section through south Séítah yields an estimate of 800 m length and ∼50 m amplitude, plotted here as a single point. The purple area denotes the Gaspé dome structure in (Figure 3) with an interpreted fold length of ∼0.5–1.5 km and a vertical relief ranging from a conservative minimum of 15 m to a more representative ∼36 m, derived from the difference in elevation between the elevation of the Séítah formation in the central part of the inlier and its flanks. The amplitude values derived from the topographic analysis in Figure 3 are considered conservative and likely underestimate the true structural relief of the structure expressed by the Gaspé outcrop. As with the south Séítah transect cross-section of Séítah, these values may underestimate amplitude by up to an order of magnitude. Nevertheless, the resulting data plots well within the range of terrestrial analogs of intrusion-related uplift structures.

Both the Séítah and Gaspé structures plot within the main trend defined by forced folds associated with thin, laterally extensive intrusions, particularly saucer-shaped sills and hybrid sill-laccoliths. The location of Séítah in this parameter space supports an interpretation of magmatic uplift associated with shallow subsurface intrusion. This is further supported by the symmetry of the dome, the absence of collapse or vent structures, and the structural architecture observed in orbital topography and rover-based cross-sections. Similar morphologies have been observed in terrestrial volcanic provinces and sedimentary basins (e.g., Magee et al., 2017), and in comparative planetary settings such as the Moon and Mars (Poppe et al., 2024), where low surface gravity and rheological layering promote fold amplification above non-eruptive intrusions.

Near fold crests, amplitude can approach total sill thickness in predominantly elastic structures, whereas margins may show shear-style strain (Magee et al., 2017); Séítah's preserved flat crest and lack of pervasive faulting argue for behavior near the elastic end-member. Geometry-based estimates point to very shallow emplacement of the causative intrusion (10–100s of meters): (a) The sill-laccolith transition in thin-plate bending occurs when half-length is ∼3–3.2 times the roof's effective elastic thickness (Pollard & Johnson, 1973). We approximate Séítah's effective elastic thickness to be roughly equal to half the fold wavelength ∼0.5 km, which would yield a lower bound on roof depth of ∼0.16 km. (b) Conservative fold diameter:depth ratios from 3D seismic analogs are typically ∼5–10 for shallow saucer/laccolith sills (Hansen & Cartwright, 2006; Jackson et al., 2013). If we imply a similar ratio for Martian examples, we would expect a depth range of ∼80–240 m for the intrusion that formed Séítah's 0.8–1.2 km dome. We therefore adopt ∼120–180 m as a best-estimate minimum depth to the intrusion

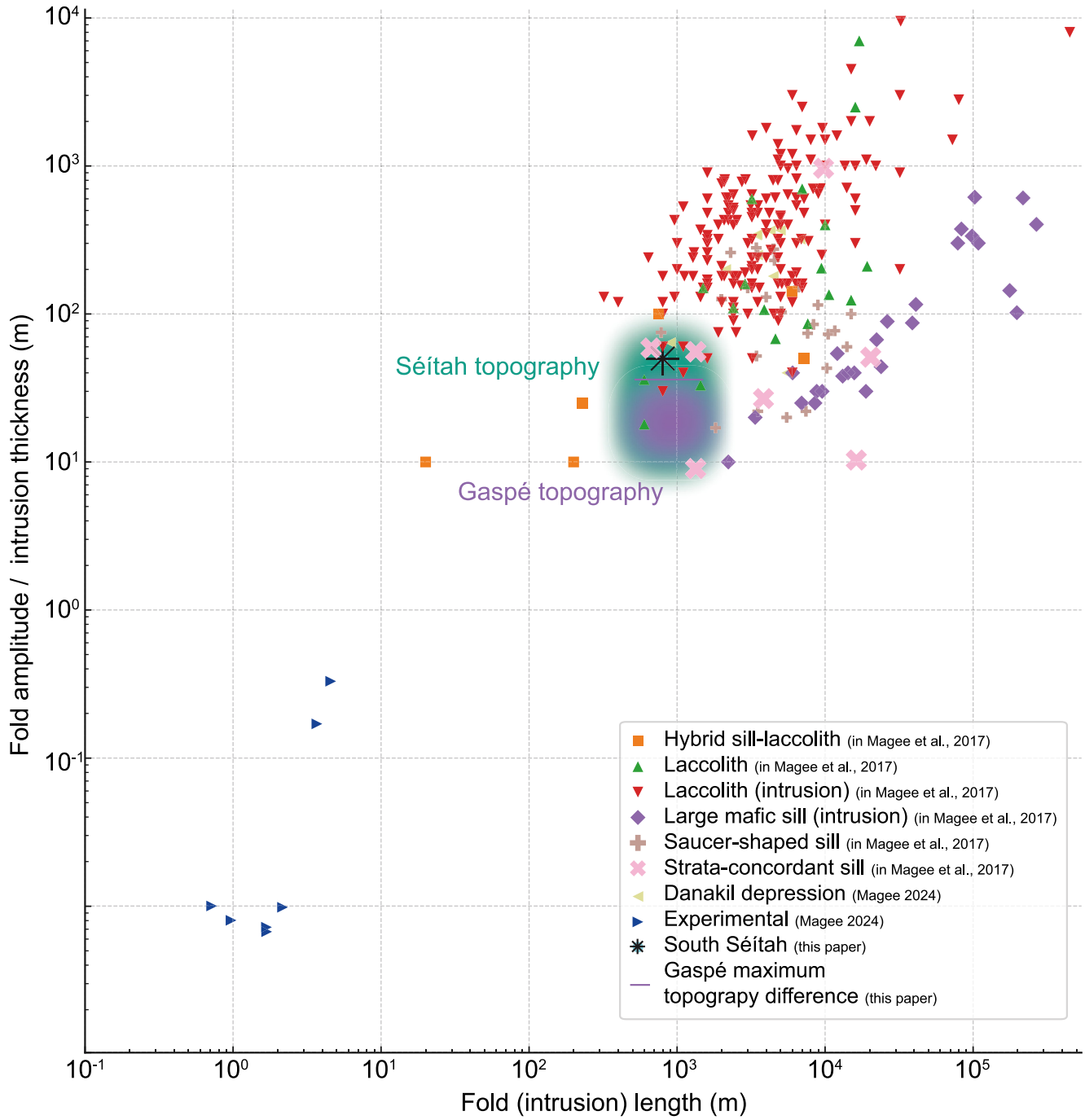

Figure 17. Log–log plot of fold amplitude or intrusion thickness versus fold/intrusion length. Data are compiled from natural and modeled examples of forced folds (Magee, 2024; Magee et al., 2017), including 3D seismic interpretations of sills and laccoliths. Shaded areas mark the estimated fold dimensions of the Séítah dome (green) and Gaspé structure (purple). The Séítah cross-section point (800 m length, 50 m amplitude) is shown as a solid marker. Both structures fall within the observed range of intrusion-related uplift, supporting their interpretation as magmatic forced folds.

roof beneath south Séítah, acknowledging that inelastic accommodation likely occurred somewhere and that this value is likely an underestimate. We have sketched an approximation of these relationships in Figure 16d, showing how a potential intrusion that has deformed the roof through predominantly elastic strain may appear based on surface observations. These depth estimates rely solely on geometric scaling; adding elastic-plate parameters such as Youngs Modulus and Poisson's ratio via flexural length-scale inversions (Michaut, 2011) is

possible but would require additional assumptions for Martian crustal properties and density contrasts, which we avoid here to keep the estimate conservative.

Together, these relationships provide a quantitative framework for interpreting Séítah as a magmatic forced fold—uplift as an elastic response to sill emplacement in the upper ~200 m of the crust of Jezero crater. The Séítah dome geometry is consistent with the behavior of terrestrial analogs, extending the applicability of intrusion-fold scaling laws to martian volcanic terrains.

7.8. A Conceptual Model to Explain Deformation of the Séítah Formation

The Séítah dome in the outcrop exhibits a lobate planform morphology and central elevation high that are consistent with formation by underlying composite intrusions built from multiple magmatic pulses, though this is difficult to test with rover data. 3D seismic examples (Kumar et al., 2022; Polteau et al., 2008; Reynolds et al., 2022) show that such complexes produce forced folds with variable orientations and plunges in different lobes.

We present a model for the development of the Séítah formation on the Jezero crater floor, which satisfies all the requirements laid out in the introduction to this section (Figure 18). The Séítah formation is stratigraphically the lowest exposed unit on the Jezero crater floor investigated by the *Perseverance* science team. It is interpreted as a coarsely crystalline olivine-rich cumulate igneous rock formed from an ultrabasic melt based on textural, mineralogical and geochemistry evidence from the strongly layered Bastide member of the formation (Farley et al., 2022; Liu et al., 2022; Treiman et al., 2025; Wiens et al., 2022). The overlying Máaz formation, which has an augite and plagioclase mineralogy, is interpreted to be either younger basaltic lava flows or a less mafic complement to the cumulate rocks of the Séítah formation (Bell et al., 2022; Farley et al., 2022; Horgan et al., 2023; Udry et al., 2023; Wiens et al., 2022). At the time of Máaz deposition, we propose that both units were broadly flat-lying (Figure 18). There is some evidence in RIMFAX profiles collected during the Rapid Traverse that upper members of the Máaz formation may have been deposited after an initial phase of uplift due to interpreted shallower dips in the upper (Naat'áanii and Ch'ał) members (Crumpler et al., 2023; Horgan et al., 2023), though outcrop descriptions describe these rocks as structureless, preventing surface confirmation of these dips in northwest Séítah (Bell et al., 2022).

One alternative is that the Séítah formation represents a sill emplaced beneath or within, and therefore post-dates the Máaz formation. Such a sill would need to extend across much of the crater floor, at least covering the present-day extent of the Séítah and Gaspé outcrops (Figures 1 and 3), with layering reflecting multiple intrusive pulses (Polteau et al., 2008; Reynolds et al., 2022). The absence of clear contact metamorphism at the base of Máaz and the chilled margin in the Séítah formation outcrops close to the contact, argues against this, though these baked and chilled margins may be too small to have been observed, obscured by regolith or removed by later alteration. Conversely, the observed stratiform textures are also compatible with a cumulate origin, where layering records magmatic differentiation during prolonged emplacement (Farley et al., 2022). Both interpretations remain viable, but in either case, the geometries of the Séítah–Máaz contact indicate initial subhorizontal, parallel emplacement. Thickness variations in the upper Maaz members, where radar reflectors and surface geometries show less rotation than in the underlying Rochette and Artuby members (Horgan et al., 2023; Thackston et al., 2024), suggest that fold amplification may have migrated across the structure. In this scenario, uplift in the northern sector occurred later than in southern Séítah, coinciding with or slightly predating the emplacement of the Naat'áanii and Ch'a volcanic members of the Máaz formation. The timing of deformation could be further constrained by comparing analyses of returned samples from the Rochette and Artuby members, the Ch'a member at Ha'ahóni and Atsá, and upper Séítah Robine and Malay samples at Issole (Simon et al., 2023; Sun et al., 2023).

Inflation of the large sill or small laccolith at shallow depths under the Séítah formation uplifted the overburden forming a ~1 km wide approximately symmetrical fold with crestal amplitude <50 m, with higher elevations of the Séítah formation in the inlier core. This folding is evidenced by the progressively increasing dips measured in the south Séítah transect from northeast to southwest. The horizontal dips estimated from image mosaics and RIMFAX radargrams in the Máaz formation define the limits of the fold structure. Overall, the dip and strike measurements collected in the south Séítah transect describe the southwest limb of an upright gentle fold with a broad, flat crest. Comparable dip magnitudes and azimuths above and below the contact between the Séítah and Máaz formations indicate that both stratigraphic units were initially deposited in largely horizontal layers and have been deformed and subsequently eroded to create the outcrop geometry we see at the present day. The fold margins correspond to intrusion edges. Intrusion geometry may have been multi-lobed (Reynolds et al., 2022),

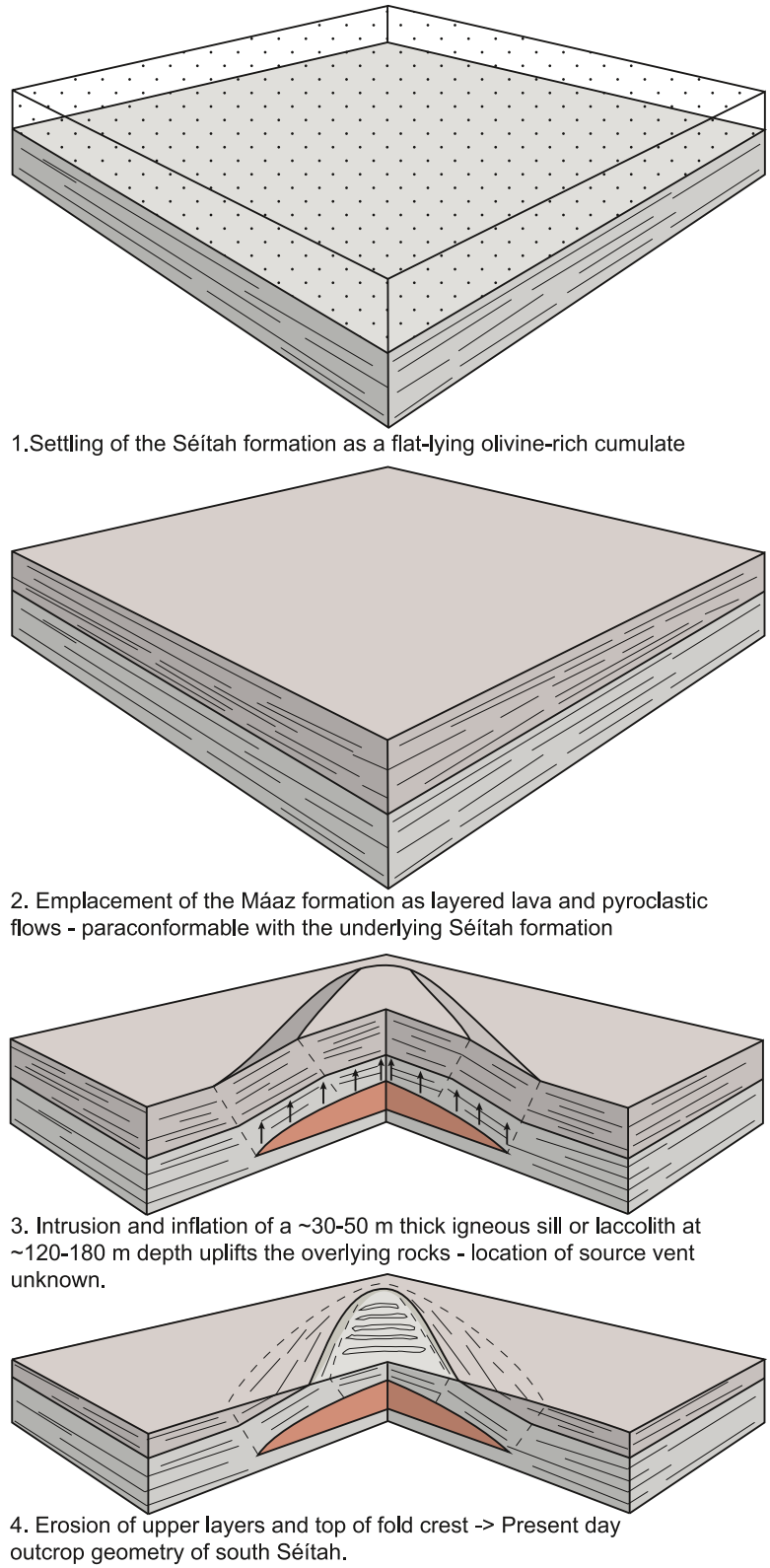

Figure 18. Sequential model for the formation of the South Séítah inlier.

with lobes fed sequentially from a central source (John & Blundy, 1993), the location of which is unknown but may underlie the central part of the Séítah dome. The along-strike decay of the limb dip (Citadelle-Artuby-Mure) and the lobate planform are consistent with incremental inflation by multiple sill lobes. Seismic and geodetic analyses show that forced folds grow in steps, recording hinge migration, up-section amplitude changes, and uplift-subsidence cycles as sill segments inflate and deflate (Magee et al., 2017; Reeves et al., 2018). We infer a similar multi-pulse history at Séítah to explain the observed lobate planform geometry of the Seitah outcrop, plunge variations and limb-dip gradients.

8. Conclusions

Comprehensive investigation of the Séítah and Máaz formations using Mastcam-Z image and 3D outcrop model data, as well as RIMFAX ground-penetrating radar data has led to a robust interpretation of the structural geometry and emplacement history of Jezero crater floor units. Our key conclusions are:

1. Kilometer-scale folding of crater floor units: The Séítah and overlying Máaz formations display a consistent pattern of bedding dip variations that are best explained by gentle folding. The geometry of this fold is asymmetric, with southwest- and northeast-dipping limbs and a sub-horizontal crestal zone forming a broad domal uplift. The folding is localized, as evidenced by steeper dips at the margins and flat-lying strata in the fold crest.
2. Simultaneous deformation of Séítah and Máaz formations: Concordant dips in both formations near their contact, and a lack of angular unconformity or truncation, indicate that the deformation post-dates the emplacement of both units. This suggests that the folding event may have affected at least the earliest emplaced members of the Máaz formation, as well as the Séítah formation.
3. Topographic-stratigraphic inversion: The elevated topography of the Séítah formation relative to the stratigraphically overlying Máaz formation is explained by fold-induced uplift of the Séítah unit. This resolves the observation that the older Séítah rocks sit topographically above the younger Máaz lava.
4. Intrusion-related forced folding: The folding is interpreted as the result of a subsurface igneous intrusion, likely a sill or laccolith, emplaced beneath the Séítah formation. The observed fold geometry, structural relief (∼30–50 m), and lateral extent (∼1 km) are consistent with deformation driven by shallow magmatic inflation with a roof estimated to be ∼120–180 below the present-day fold crest. The absence of associated faulting, fluidization, or compaction features supports the mechanism of elastic flexure above an intrusive body.
5. Implications for Martian magmatic processes: The structural evidence for intrusion-driven deformation adds a new dimension to our understanding of Martian igneous systems. This supports the hypothesis that the Séítah formation may represent not only a cumulate body but also the roof of a larger intrusive complex, potentially contributing to the petrogenesis of both the Séítah and Máaz formations.

This study provides the first in situ evidence of forced folding related to magmatic intrusion on Mars and demonstrates the utility of combining stereo-imaging, 3D modeling, and subsurface radar sounding to unravel the structural history of planetary surfaces. Future work should aim to map the full extent of similar folds within the Jezero crater floor to constrain the size and morphology of possible underlying igneous bodies.

Conflict of Interest

The authors declare no conflicts of interest relevant to this study.

Availability Statement

The data used in this publication are from the Mastcam-Z (Bell & Maki, 2021), Navcam (Maki et al., 2020), instruments on the Mars2020 *Perseverance* rover, the RTE camera on board the *Ingenuity* helicopter (Balaram et al., 2021), and the HiRISE instrument on the Mars Reconnaissance Orbiter (McEwen et al., 2007). All *Perseverance* data products used here are archived in the Planetary Data System Imaging node (https://pds-imaging.jpl.nasa.gov/volumes/mars2020.html) [Dataset] and the Geosciences node [Dataset] (https://pds-geosciences.wustl.edu/missions/mars2020/). Mars 2,020 Mastcam-Z source images are available on https://mars.nasa.gov/mars2020/multimedia/raw-images/ (Mastcam-Z, Bell & Maki, 2021) [Dataset]. Mastcam-Z data used in this study are available via this database: Bell and Maki (2021; [Data] https://doi.org/10.17189/1522843, or via the Mastcam-Z public website mosaic page (https://mastcamz.asu.edu/mars-images/panoramas-mosaics/) [Dataset]. Ordered Point Clouds (OPCs) as processed by PRoViP from all PDS-released Mastcam-Z stereo and monoscopic

data sets are available from sftp://PRoViP-Mastcam-Z-PDS-Released@dig-sftp.joanneum.at:2200—with user PRoViP-Mastcam-Z-PDS Released and password MQRr63hJdUzVFHYc! The one-click access link is sftp://PRoViP-MastcamZ-PDS-Released:MQRr63hJdUzVFHYc!@dig-sftp.joanneum.at:2200/. [Dataset] An OPC from HiRISE DTM/Ortho (monochrome) is available on sftp://PRoVi-OpenAccess@dig-sftp.joanneum.at/Mars/MARS-2020/HiRISE/OPC — with user PRoVi-OpenAccess and password LMWasdwd!201423!g. The one-click access link is sftp://PRoVi-OpenAccess:LMWasdwd!201423!g@dig-sftp.joanneum.at/Mars/MARS-2020/HiRISE/OPC/. OPCs from MSL Mastcam stereo data are available from dig-sftp.joanneum.at—with user MSL and password WH549!bjABu. The one-click access link is sftp://MSL:WH549!bjABu@dig-sftp.joanneum.at/. [Dataset] Navcam image data is available via Maki (2020; [Data] https://doi.org/10.17189/d3nm-pp09); [Dataset], and *Ingenuity* data is available via Balaram (2021; [Data] https://doi.org/10.17189/1522845); [Dataset]. VRVis PRo3D: a 3D viewer for exploration and geologic interpretation of planetary surface reconstructions. (2025, April 02; Version 5.0.0) [Software]. https://github.com/pro3d-space/PRo3D/ Details about the software can be found at: https://pro3d.space/ (Paar et al., 2023).

Acknowledgments

The authors wish to thank the Mars 2020 science and engineering teams for their hard work in tactical and strategic science operations. We also wish to pay particular thanks to the Mars 2020 project management and campaign science leads for their efforts in making the mission a success, as well as the Mastcam-Z, operations teams for their investment in the mission and in acquiring the data products used here. We thank Craig Magee and an anonymous reviewer for their insightful and constructive suggestions, which helped refine the manuscript. RB and SG acknowledge the UK Space Agency for funding this project (Grant refs: ST/Y000153/1, ST/T001755/1, ST/X002373/1). JB, BH, JN, MR, were funded by JPL's Mars 2020 Project via a subcontract from the California Institute of Technology/Jet Propulsion Laboratory to Arizona State University (subcontract 1511125). This work was carried out by KF, KS, JM, SS, and VS at the Jet Propulsion Laboratory, California Institute of Technology, under a contract with the National Aeronautics and Space Administration (80NM0018D0004). JIS acknowledges funding from JPL's Science Mission Directorate and Mars Exploration Program. DF acknowledges funding from the Australian Research Council. OB was supported by the French Space Agency CNES.

References

Agirrezabala, L. M. (2015). Syndepositional forced folding and related fluid plumbing above a magmatic laccolith: Insights from outcrop (Lower Cretaceous, Basque-Cantabrian Basin, Western Pyrenees). *GSA Bulletin*, *127*(7–8), 982–1000.

Alwmark, S., Horgan, B., Udry, A., Bechtold, A., Fagents, S., Ravanis, E., et al. (2023). Diverse lava flow morphologies in the stratigraphy of the Jezero crater floor. *Journal of Geophysical Research: Planets*, *128*(7), e2022JE007446. https://doi.org/10.1029/2022je007446

Balaram, J., Aung, M., & Golombek, M. P. (2021). The Ingenuity helicopter on the Perseverance rover. *Space Science Reviews*, *217*(4), 56. https://doi.org/10.1007/s11214-021-00815-w

Balme, M., Robson, E., Barnes, R., Butcher, F., Fawdon, P., Huber, B., et al. (2017). Surface-based 3D measurements of small aeolian bedforms on Mars and implications for estimating ExoMars rover traversability hazards. *Planetary and Space Science*. *153*, 39–53. https://doi.org/10.1016/j.pss.2017.12.008

Banham, S. G., Gupta, S., Rubin, D. M., Edgett, K. S., Barnes, R., Van Beek, J., et al. (2021). A rock record of complex aeolian bedforms in a Hesperian desert landscape: The Stimson formation as exposed in the Murray buttes, Gale crater, Mars. *Journal of Geophysical Research: Planets*, *126*(4), e2020JE006554. https://doi.org/10.1029/2020je006554

Banham, S. G., Gupta, S., Rubin, D. M., Watkins, J. A., Sumner, D. Y., Edgett, K. S., et al. (2018). Ancient Martian aeolian processes and palaeomorphology reconstructed from the Stimson formation on the lower slope of Aeolis Mons, Gale crater, Mars. *Sedimentology*, *65*(4), 993–1042. https://doi.org/10.1111/sed.12469

Barnes, R., Gupta, S., Traxler, C., Ortner, T., Bauer, A., Hesina, G., et al. (2018). Geological analysis of Martian rover-derived Digital Outcrop Models using the 3D visualisation tool, Planetary Robotics 3D Viewer–PRo3D. *Earth and Space Science*, *5*(2018), 285–307. https://doi.org/10.1002/2018ea000374

Bell, J. F., & Maki, J. M. (2021). Mars 2020 Mast Camera Zoom bundle [Dataset]. https://doi.org/10.17189/1522843

Bell, J. F., Maki, J. N., Mehall, G. L., Ravine, M. A., Caplinger, M. A., Bailey, Z. J., et al. (2021). The Mars 2020 perseverance rover Mast Camera Zoom (Mastcam-Z) multispectral, stereoscopic imaging investigation. *Space Science Reviews*, *217*(1), 24. https://doi.org/10.1007/s11214-020-00755-x

Bell III, J. F., Maki, J. N., Alwmark, S., Ehlmann, B. L., Fagents, S. A., Grotzinger, J. P., et al. (2022). Geological, multispectral, and meteorological imaging results from the Mars 2020 Perseverance rover in Jezero crater. *Science Advances*, *8*(47), eabo4856. https://doi.org/10.1126/sciadv.abo4856

Beyssac, O., Forni, O., Cousin, A., Udry, A., Kah, L. C., Mandon, L. E. C. Y. L., et al. (2023). Petrological traverse of the olivine cumulate Séítah formation at Jezero crater, Mars: A perspective from SuperCam onboard Perseverance. *Journal of Geophysical Research: Planets*, *128*(7), e2022JE007638. https://doi.org/10.1029/2022je007638

Bilotti, F., & Shaw, J. H. (2005). Deep-water Niger Delta fold and thrust belt modeled as a critical-taper wedge: The influence of elevated basal fluid pressure on structural styles. *AAPG Bulletin*, *89*(11), 1475–1491. https://doi.org/10.1306/06130505002

Braathen, A., Petrie, E., Nystuen, T., Sundal, A., Skurtveit, E., Zuchuat, V., et al. (2020). Interaction of deformation bands and fractures during progressive strain in monocline-San Rafael Swell, Central Utah, USA. *Journal of Structural Geology*, *141*, 104219. https://doi.org/10.1016/j.jsg.2020.104219

Briggs, S. E., Davies, R. J., Cartwright, J. A., & Morgan, R. (2006). Multiple detachment levels and their control on fold styles in the compressional domain of the deepwater west Niger Delta. *Basin Research*, *18*(4), 435–450. https://doi.org/10.1111/j.1365-2117.2006.00300.x

Bunger, A. P., & Cruden, A. R. (2011). Modeling the growth of laccoliths and large mafic sills: Role of magma body forces. *Journal of Geophysical Research*, *116*(B2), B02203. https://doi.org/10.1029/2010JB007648

Buxtorf, A. (1916). Prognosen und Befunde beim Hauensteinbasis-und Grenchenbergtunnel und die Bedeutung der letzteren für die Geologie des Juragebirges. *Verhandlungen der Naturforschenden Gesellschaft in Basel*, *27*, 184–254.

Casciello, E., Vergés, J., Saura, E., Casini, G., Fernández, N., Blanc, E., et al. (2009). Fold patterns and multilayer rheology of the Lurestan Province, Zagros simply folded belt (Iran). *Journal of the Geological Society*, *166*(5), 947–959. https://doi.org/10.1144/0016-76492008-138

Corredor, F., Shaw, J. H., & Bilotti, F. (2005). Structural styles in the deep-water fold and thrust belts of the Niger Delta. *AAPG Bulletin*, *89*(6), 753–780. https://doi.org/10.1306/02170504074

Corry, C. E. (1988). Laccoliths: Mechanics of emplacement and growth. *Geological Society of America Special Paper*, *220*, 110. https://doi.org/10.1130/SPE220

Cosgrove, J., & Ameen, M. (1999). A comparison of the geometry, spatial organization and fracture patterns associated with forced folds and buckle folds. *Geological Society, London, Special Publications*, *169*(1), 7–21. https://doi.org/10.1144/gsl.sp.2000.169.01.02

Cosgrove, J. W., & Hillier, R. D. (1999). Forced-fold development within tertiary sediments of the Alba Field, UKCS: Evidence of differential compaction and post-depositional sandstone remobilization. *Geological Society London, Special Publications*, *169*, 61–71. https://doi.org/10.1144/gsl.sp.2000.169.01.05

Crumpler, L. S., Horgan, B. H. N., Simon, J. I., Stack, K. M., Alwmark, S., Dromart, G., et al. (2023). In situ geologic context mapping transect on the floor of Jezero Crater from Mars 2020 Perseverance rover observations. *Journal of Geophysical Research: Planets*, *128*(10), e2022JE007444. https://doi.org/10.1029/2022je007444

Ehlmann, B. L., Mustard, J. F., Murchie, S. L., Poulet, F., Bishop, J. L., Brown, A. J., et al. (2008). Orbital identification of carbonate-bearing rocks on Mars. *Science*, *322*(5909), 1828–1832. https://doi.org/10.1126/science.1164759

Epard, J.-L., & Groshong Jr, R. H. (1993). Excess area and depth to detachment. *AAPG Bulletin*, *77*(8), 1291–1302.

Erslev, E. A. (1991). Trishear fault-propagation folding. *Geology*, *19*(6), 617–620. https://doi.org/10.1130/0091-7613(1991)019<0617:tfpf>2.3.co;2

Evans, A. D., Teagle, D. A. H., Craw, D., Henstock, T. J., & Falcon-Suarez, I. H. (2021). Uplift and exposure of serpentinized massifs: Modeling differential serpentinite diapirism and exhumation of the Troodos Mantle Sequence, Cyprus. *Journal of Geophysical Research: Solid Earth*, *126*(6), e2020JB021079. https://doi.org/10.1029/2020JB021079

Farley, K. A., Stack, K. M., Shuster, D. L., Horgan, B. H. N., Hurowitz, J. A., Tarnas, J. D., et al. (2022). Aqueously altered igneous rocks sampled on the floor of Jezero crater, Mars. *Science*, *377*(6614), eabo2196. https://doi.org/10.1126/science.abo2196

Farley, K. A., Williford, K. H., Stack, K. M., Bhartia, R., Chen, A., de la Torre, M., et al. (2020). Mars 2020 Mission Overview. *Space Science Reviews*, *216*(8), 142. https://doi.org/10.1007/s11214-020-00762-y

Fletcher, R. C. (1991). Three-dimensional folding of an embedded viscous layer in pure shear. *Journal of Structural Geology*, *13*(1), 87–96. https://doi.org/10.1016/0191-8141(91)90103-p

Galland, O., Burchardt, S., Hallot, E., Mourgues, R., & Bulois, C. (2014). Dynamics of shallow magmatic systems: Laboratory models of sill and laccolith emplacement. *Geological Society of America Bulletin*, *126*(1–2), 3–18. https://doi.org/10.1130/B30898.1

Galland, O., de la Cal, H., Mescua, J., & Rabbel, O. (2022). 3-dimensional trapdoor structure of laccolith-induced doming and implications for laccolith emplacement, Pampa Amarilla, Mendoza Province, Argentina. *Tectonophysics*, *836*, 229418. https://doi.org/10.1016/j.tecto.2022.229418

Galland, O., Spacapan, J. B., Rabbel, O., Mair, K., González Soto, F., Eiken, T., et al. (2019). Structure, emplacement mechanism and magma-flow significance of igneous fingers – Implications for sill emplacement in sedimentary basins. *Journal of Structural Geology*, *124*, 120–135. https://doi.org/10.1016/j.jsg.2019.04.013

Germanovich, L. N., Genc, G., Lowell, R. P., & Rona, P. A. (2012). Deformation and surface uplift associated with serpentinization at mid-ocean ridges and subduction zones. *Journal of Geophysical Research*, *117*, B07103. https://doi.org/10.1029/2012JB00937

Goudge, T. A., Mustard, J. F., Head, J. W., Fassett, C. I., & Wiseman, S. M. (2015). Assessing the mineralogy of the watershed and fan deposits of the Jezero crater paleolake system, Mars. *Journal of Geophysical Research: Planets*, *120*(4), 775–808. https://doi.org/10.1002/2014je004782

Gudmundsson, A. (2011). Deflection of dykes into sills at discontinuities and magma-chamber formation. *Tectonophysics*, *500*(1–4), 50–64. https://doi.org/10.1016/j.tecto.2009.10.015

Hamran, S.-E., Paige, D. A., Allwood, A., Amundsen, H. E. F., Berger, T., Brovoll, S., et al. (2022). Ground penetrating radar observations of subsurface structures in the floor of Jezero crater, Mars. *Science Advances*, *8*(34), eabp8564. https://doi.org/10.1126/sciadv.abp8564

Hansen, D. M., & Cartwright, J. (2006). The three-dimensional geometry and growth of forced folds above saucer-shaped igneous sills. *Journal of Structural Geology*, *28*(8), 1520–1535. https://doi.org/10.1016/j.jsg.2006.04.004

Hansen, D. M., Cartwright, J., & Huuse, M. (2008). 3D seismic analysis of the geometry of igneous sills and forced folds in the Faroe–Shetland Basin. *Basin Research*, *20*, 153–179. https://doi.org/10.1111/j.1365-2117.2008.00351.x

Harding, T. P. (1985). Seismic characteristics and identification of negative flower structures, positive flower structures, and positive structural inversion. *AAPG Bulletin*, *69*(4), 582–600. https://doi.org/10.1306/AD462538-16F7-11D7-8645000102C1865D

Hardy, S., & McClay, K. (1999). Kinematic modelling of extensional fault-propagation folding. *Journal of Structural Geology*, *21*(7), 695–702. https://doi.org/10.1016/s0191-8141(99)00072-3

Hayes, A. G., Corlies, P., Tate, C., Barrington, M., Bell, J. F., Maki, J. N., et al. (2021). Pre-flight calibration of the Mars 2020 Rover Mastcam Zoom (Mastcam-Z) multispectral, stereoscopic imager. *Space Science Reviews*, *217*(2), 1–95. https://doi.org/10.1007/s11214-021-00795-x

Hernández-Montenegro, J. D., Kizovski, T. V., Treiman, A. H., Li, A. Y., Asimow, P. D., Schmidt, M. E., et al. (2025). Petrogenesis of the olivine cumulate outcrop Issole–The missing link between the Séítah and Máaz formations in jezero crater, Mars. *Icarus*, *437*, 116620. https://doi.org/10.1016/j.icarus.2025.116620

Homza, T. X., & Wallace, W. K. (1995). Geometric and kinematic models for detachment folds with fixed and variable detachment depths. *Journal of Structural Geology*, *17*(4), 575–588. https://doi.org/10.1016/0191-8141(94)00077-d

Horgan, B., Udry, A., Rice, M., Alwmark, S., Amundsen, H. E. F., Bell, J. F. I. I. I., et al. (2023). Mineralogy, morphology, and emplacement history of the maaz formation on the jezero crater floor from orbital and rover observations. *Journal of Geophysical Research: Planets*, *128*(8), e2022JE007612. https://doi.org/10.1029/2022JE007612

Hudleston, P. J., & Treagus, S. H. (2010). Information from folds: A review. *Journal of Structural Geology*, *32*(12), 2042–2071. https://doi.org/10.1016/j.jsg.2010.08.011

Hunt, C. B. (1953). *Geology and geography of the Henry Mountains region*. U.S. Geological Survey Professional Paper, (Vol. 228, p. 234). https://doi.org/10.3133/pp228

Jackson, C. A., Schofield, N., & Golenkov, B. (2013). Geometry and controls on the development of igneous sill–related forced folds: A 2-D seismic reflection case study from offshore southern Australia. *GSA Bulletin*, *125*(11–12), 1874–1890. https://doi.org/10.1130/b30833.1

John, B. E., & Blundy, J. D. (1993). Emplacement-related deformation of granitoid magmas, southern Adamello Massif, Italy. *Geological Society of America Bulletin*, *105*(12), 1517–1541. https://doi.org/10.1130/0016-7606(1993)105<1517:erdogm>2.3.co;2

Johnson, A. M., & Pollard, D. D. (1973). Mechanics of growth of some laccolithic intrusions in the Henry mountains, Utah, I: Field observations, Gilbert's model, physical properties and flow of the magma. *Tectonophysics*, *18*(3–4), 261–309. https://doi.org/10.1016/0040-1951(73)90050-4

Johnson, R. B. (1968). *Geology of the igneous rocks of the Spanish Peaks region, Colorado*. US Government Printing Office.

Jolly, B. A., Lonergan, L., & Whittaker, A. C. (2016). Growth history of fault-related folds and interaction with seabed channels in the toe-thrust region of the deep-water Niger delta. *Marine and Petroleum Geology*, *70*, 58–76. https://doi.org/10.1016/j.marpetgeo.2015.11.003

Kenkmann, T. (2002). Folding within seconds. *Geology*, *30*(3), 231–234. https://doi.org/10.1130/0091-7613(2002)030<0231:fws>2.0.co;2

Kenkmann, T., Collins, G. S., Wünnemann, K., Osinski, G., & Pierazzo, E. (2013). The modification stage of crater formation. In G. R., Osinski, & E. Pierazzo (Ed.), *Impact cratering: Processes and Products*, 60–75. https://doi.org/10.1002/9781118447307

Kenkmann, T., Poelchau, M. H., & Wulf, G. (2014). Structural geology of impact craters. *Journal of Structural Geology*, *62*, 156–182. https://doi.org/10.1016/j.jsg.2014.01.015

Kenkmann, T., & von Dalwigk, I. (2000). Radial transpression ridges: A new structural feature of complex impact craters. *Meteoritics & Planetary Sciences*, *35*(6), 1189–1201. https://doi.org/10.1111/j.1945-5100.2000.tb01508.x

Kinch, K. M., Madsen, M. B., Bell, J. F., III, Maki, J. N., Bailey, Z., Hayes, A. G., et al. (2020). Radiometric calibration targets for the Mastcam-Z camera on the Mars 2020 rover mission. *Space Science Reviews*, *216*(8), 141. https://doi.org/10.1007/s11214-020-00774-8

Kremer, C. H., Mustard, J. F., & Bramble, M. S. (2019). A widespread olivine-rich ash deposit on Mars. *Geology*, *47*(7), 677–681. https://doi.org/10.1130/g45563.1

Kumar, P. C., Niyazi, Y., Eruteya, O. E., Moscariello, A., Warne, M., Ierodiaconou, D., & Sain, K. (2022). Anatomy of intrusion related forced fold in the offshore Otway Basin, SE Australia. *Marine and Petroleum Geology*, *141*, 105719. https://doi.org/10.1016/j.marpetgeo.2022.105719

Leuthold, J., Müntener, O., Baumgartner, L., Putlitz, B., Ovtcharova, M., & Schaltegger, U. (2012). Time resolved construction of a bimodal laccolith (Torres del Paine, Patagonia). *Earth and Planetary Science Letters*, *325–326*, 85–92. https://doi.org/10.1016/j.epsl.2012.01.032

Leuthold, J., Müntener, O., Baumgartner, L., Putlitz, B., Ovtcharova, M., & Schaltegger, U. (2013). The Torres del Paine Mafic Complex (Patagonia). *Journal of Petrology*, *54*(2), 273–303. https://doi.org/10.1093/petrology/egs069

Lewis, M. M., Jackson, C. A.-L., Gawthorpe, R. L., & Whipp, P. S. (2015). Early synrift reservoir development on the flanks of extensional forced folds: A seismic-scale outcrop analog from the Hadahid fault system, Suez rift, Egypt, Early synrift Reservoir Development. *AAPG Bulletin*, *99*(6), 985–1012. https://doi.org/10.1306/120111414036

Lino, L. M., & Vlach, S. R. F. (2021). Textural and geochemical evidence for multiple, sheet-like magma pulses in the Limeira intrusion, Paraná Magmatic Province, Brazil. *Journal of Petrology*, *62*(3), egab011. https://doi.org/10.1093/petrology/egab011

Liu, Y., Tice, M. M., Schmidt, M. E., Treiman, A. H., Kizovski, T. V., Hurowitz, J. A., et al. (2022). An olivine cumulate outcrop on the floor of Jezero crater, Mars. *Science*, *377*(6614), 1513–1519.

Magee, C. (2024). Fractures and faults across intrusion-induced forced folds: A georesource perspective. https://doi.org/10.1144/SP547-2023-47

Magee, C., Briggs, F., & Jackson, C. A.-L. (2013). Lithological controls on igneous intrusion-induced ground deformation. *Journal of the Geological Society*, *170*(6), 853–856. https://doi.org/10.1144/jgs2013-029

Magee, C., Hoggett, M., Jackson, C. A. L., & Jones, S. M. (2019). Burial-related compaction modifies intrusion-induced forced folds: Implications for reconciling roof uplift mechanisms using seismic reflection data. *Frontiers in Earth Science*, *7*, 37.

Magee, C., Jackson, C. A.-L., Hardman, J. P., & Reeve, M. T. (2017). Decoding sill emplacement and forced fold growth in the Exmouth Sub-basin, offshore northwest Australia: Implications for hydrocarbon exploration. *Interpretation*, *5*(3), SK11–SK22. https://doi.org/10.1190/int-2016-0133.1

Magee, C., Jackson, C. A. L., & Schofield, N. (2014). The influence of normal fault geometry on igneous sill emplacement and morphology. *Geology*, *42*, 323–326. https://doi.org/10.1130/G35150.1

Magee, C., Pichel, L. M., Madden-Nadeau, A. L., Jackson, C. A. L., & Mohriak, W. (2021). Salt–magma interactions influence intrusion distribution and salt tectonics in the Santos Basin, offshore Brazil. *Basin Research*, *33*(3), 1820–1843. https://doi.org/10.1111/bre.12537

Maki, J. N., Gruel, D., McKinney, C., Ravine, M. A., Morales, M., Lee, D., et al. (2020). The Mars 2020 Engineering Cameras and Microphone on the Perseverance rover: A Next-Generation Imaging System for Mars exploration. *Space Science Reviews*, *216*(8), 137. https://doi.org/10.1007/s11214-020-00765-9

Mandon, L., Quantin-Nataf, C., Thollot, P., Mangold, N., Lozac'h, L., Dromart, G., et al. (2020). Refining the age, emplacement and alteration scenarios of the olivine-rich unit in the Nili Fossae region, Mars. *Icarus*, *336*, 113436. https://doi.org/10.1016/j.icarus.2019.113436

McClay, K. R. (1987). The mapping of geological structures. In *Geological Society of London Handbook*. Open University Press.

McEwen, A. S., Eliason, E. M., Bergstrom, J. W., Bridges, N. T., Hansen, C. J., Delamere, W. A., et al. (2007). Mars Reconnaissance Orbiter's High Resolution Imaging Science Experiment (HiRISE). *Journal of Geophysical Research*, *112*(E). https://doi.org/10.1029/2005JE002605

Menand, T. (2011). Physical controls and depth of emplacement of igneous bodies: A review. *Tectonophysics*, *500*(1–4), 11–19. https://doi.org/10.1016/j.tecto.2009.10.016

Michaut, C. (2011). Dynamics of magmatic intrusions in the upper crust: Theory and applications to laccoliths on Earth and the moon. *JGR: Solid Earth*, *116*(B5), B05205. https://doi.org/10.1029/2010jb008108

Michel, J., Baumgartner, L., Putlitz, B., Schaltegger, U., & Ovtcharova, M. (2008). Incremental growth of the Patagonian Torres del Paine laccolith over 90 k.y. *Geology*, *36*(6), 459–462. https://doi.org/10.1130/G24546A.1

Mitra, G., & Marshak, S. (1988). *Basic Methods of Structural Geology*. *Prentice Hall*.

Mitra, S. (2003). A unified kinematic model for the evolution of detachment folds. *Journal of Structural Geology*, *25*(10), 1659–1673. https://doi.org/10.1016/s0191-8141(02)00198-0

Montanari, D., Bonini, M., Corti, G., Agostini, A., & Del Ventisette, C. (2017). Forced folding above shallow magma intrusions: Insights on supercritical fluid flow from analogue modelling. *Journal of Volcanology and Geothermal Research*, *345*, 67–80. https://doi.org/10.1016/j.jvolgeores.2017.07.022

Morgan, S., Stanik, A., Horsman, E., Tikoff, B., de Saint-Blanquat, M., & Habert, G. (2008). Emplacement of multiple magma sheets and wall-rock deformation: Trachyte Mesa intrusion, Henry Mountains, Utah. *Journal of Structural Geology*, *30*(4), 491–512. https://doi.org/10.1016/j.jsg.2008.01.005

Omosanya, K. O., Johansen, S. E., Eruteya, O. E., & Waldmann, N. (2017). Forced folding and complex overburden deformation associated with magmatic intrusion in the Vøring Basin, offshore Norway. *Tectonophysics*, *706*, 14–34. https://doi.org/10.1016/j.tecto.2017.03.026

Ortner, T., Paar, G., Hesina, G., Tobler, R. F., & Nauschnegg, B. (2010). Towards true underground infrastructure surface documentation. In M. Schrenk, V. V. Popovich, & P. Zeile (Eds.), *Proceedings of the Real Corp 2010* (pp. 1–10).

Paar, G., Deen, R. G., Muller, J.-P., Silva, N., Iles, P., Shaukat, A., & Gao, Y. (2016). *Vision and Image Processing, Contemporary planetary robotics: An approach toward autonomous systems* (pp. 105–179). John Wiley and Sons. https://doi.org/10.1002/9783527684977.ch3

Paar, G., Ortner, T., Tate, C., Deen, R. G., Abercrombie, P., Vona, M., et al. (2023). Three-dimensional data preparation and immersive mission-spanning visualization and analysis of Mars 2020 Mastcam-Z stereo image sequences. *Earth and Space Science*, *10*(3), e2022EA002532. https://doi.org/10.1029/2022ea002532

Planke, S., Rasmussen, T., Rey, S. S., & Myklebust, R. (2005). Seismic characteristics and distribution of volcanic intrusions in the Vøring and møre basins. In D. M. Hansen & J. Cartwright (Eds.), *Volcanic rifted margins* (Vol. 234, pp. 305–321). Geological Society, London, Special Publications.

Poblet, J., & McClay, K. (1996). Geometry and kinematics of single-layer detachment folds. *AAPG Bulletin*, *80*(7), 1085–1109. https://doi.org/10.1306/64ED8CA0-1724-11D7-8645000102C1865D

Pollard, D. D., & Johnson, A. M. (1973). Mechanics of growth of some laccolithic intrusions in the henry Mountains, Utah, II: Bending and failure of overburden layers and sill formation. *Tectonophysics*, *18*(3), 311–354. https://doi.org/10.1016/0040-1951(73)90051-6

Polteau, S., Mazzini, A., Galland, O., Planke, S., & Malthe-Sørenssen, A. (2008). Saucer-shaped intrusions: Occurrences, emplacement and implications. *Earth and Planetary Science Letters*, *266*(1–2), 195–204. https://doi.org/10.1016/j.epsl.2007.11.015

Poppe, S., Wauthier, C., & Fontijn, K. (2024). Inversions of surface displacements in scaled experiments of analog magma intrusion. *Geophysical Research Letters*, *51*(8), e2023GL106805. https://doi.org/10.1029/2023gl106805

Quinn, D. P., & Ehlmann, B. L. (2019). A PCA-based framework for determining remotely sensed geological surface orientations and their statistical quality. *Earth and Space Science*, *6*(8), 1378–1408. https://doi.org/10.1029/2018ea000416

Ramsay, J. G. (1967). *Folding and fracturing of rocks* (p. 568). McGraw-Hill.

Ramsay, J. G., & Huber, M. I. (1987). *The techniques of modern structural geology, volume 2: Folds and fractures* (p. 391). Academic Press.

Reeves, J., Magee, C., & Jackson, C. A.-L. (2018). Unravelling intrusion-induced forced fold kinematics and ground deformation using 3D seismic reflection data. *Volcanica*, *1*, 1–17. https://doi.org/10.30909/VOL.01.01.0117

Reynolds, P., Holford, S., Schofield, N., & Ross, A. (2022). 3D seismic reflection constraints on the emplacement of mafic laccoliths and their role in shallow crustal magma transport: A case study from the Ceduna sub-basin, Great Australian Bight. *Marine and Petroleum Geology*, *135*, 105419. https://doi.org/10.1016/j.marpetgeo.2021.105419

Sattarzadeh, Y., Cosgrove, J., & Vita-Finzi, C. (1999). The interplay of faulting and folding during the evolution of the Zagros deformation belt. *Geological Society*, *169*, 187–196. https://doi.org/10.1144/gsl.sp.2000.169.01.14

Schofield, N., Brown, D. J., Magee, C., & Stevenson, C. T. E. (2012). Sill morphology and comparison between emplacement styles in the Faroe–Shetland Basin: Using 3D seismic data to test and refine the emplacement model. *Journal of the Geological Society, London*, *169*(2), 127–141. https://doi.org/10.1144/0016-76492011-078

Schofield, N., Stevenson, C. T. E., & Reston, T. J. (2010). Sill morphology and comparison between emplacement styles in the Faroe–Shetland Basin: Using 3D seismic data to test and refine the emplacement model. *Journal of the Geological Society, London*, *167*, 1123–1136. https://doi.org/10.1144/0016-76492010-019

Schon, S. C., Head, J. W., & Fassett, C. I. (2012). An overfilled lacustrine system and progradational delta in Jezero crater, Mars: Implications for Noachian climate. *Planetary and Space Science*, *67*(1), 28–45. https://doi.org/10.1016/j.pss.2012.02.003

Schultz, R. A., & Frey, H. V. (1990). A new survey of multiring impact basins on Mars. *Journal of Geophysical Research*, *95*(B9), 14175–14189. https://doi.org/10.1029/jb095ib09p14175

Sharp, I. R., Gawthorpe, R. L., Underhill, J. R., & Gupta, S. (2000). Fault-propagation folding in extensional settings: Examples of structural style and synrift sedimentary response from the Suez rift, Sinai, Egypt. *Geological Society of America Bulletin*, *112*(12), 1877–1899. https://doi.org/10.1130/0016-7606(2000)112<1877:fpfies>2.0.co;2

Sholes, S. F., Dickeson, Z. I., Montgomery, D. R., & Catling, D. C. (2021). Where are Mars' hypothesized ocean shorelines? Large lateral and topographic offsets between different versions of paleoshoreline maps. *Journal of Geophysical Research: Planets*, *126*(5), e2020JE006486. https://doi.org/10.1029/2020je006486

Simon, J. I., Hickman-Lewis, K., Cohen, B. A., Mayhew, L. E., Shuster, D. L., Debaille, V., et al. (2023). Samples collected from the floor of Jezero Crater with the Mars 2020 Perseverance rover. *Journal of Geophysical Research: Planets*, *128*(6), e2022JE007474. https://doi.org/10.1029/2022JE007474

Spacapan, J. B., Galland, O., Manceda, R., Senger, K., & Guldstrand, F. (2017). Roof uplift, host rock deformation and sill emplacement in the Neuquén Basin, Argentina. *Journal of Structural Geology*, *95*, 58–81. https://doi.org/10.1016/j.jsg.2016.12.004

Stack, K. M., Williams, N. R., Calef, F., Sun, V. Z., Williford, K. H., Farley, K. A., et al. (2020). Photogeologic map of the perseverance Rover Field site in jezero crater constructed by the Mars 2020 science team. *Space Science Reviews*, *216*(8), 127. https://doi.org/10.1007/s11214-020-00739-x

Stearns, D. W. (1978). *Faulting and forced folding in the Rocky Mountains foreland* (Vol. 151, pp. 1–38). Geological Society of America Memoir. https://doi.org/10.1130/mem151-p1

Sun, V. Z., Hand, K. P., Stack, K. M., Farley, K. A., Simon, J. I., Newman, C., et al. (2023). Overview and results from the Mars 2020 Perseverance rover's first science campaign on the Jezero crater floor. *Journal of Geophysical Research: Planets*, *128*(6), e2022JE007613. https://doi.org/10.1029/2022je007613

Sun, V. Z., & Stack, K. M. (2020). *Geologic map of Jezero crater and the Nili Planum region, Mars (USGS Numbered Series No. 3464). Geologic map of Jezero crater and the Nili Planum region, Mars* (Vol. 3464). U.S. Geological Survey.

Suppe, J. (1983). Geometry and kinematics of fault-bend folding. *American Journal of Science*, *283*(7), 684–721. https://doi.org/10.2475/ajs.283.7.684

Suppe, J., Chou, G. T., & Hook, S. C. (1992). Rates of folding and faulting determined from growth strata. In K. R. McClay (Ed.), *Thrust tectonics*. Springer. https://doi.org/10.1007/978-94-011-3066-0_9

Suppe, J., & Medwedeff, D. A. (1990). Geometry and kinematics of fault-propagation folding. *Eclogae Geologicae Helvetiae*, *83*(3), 409–454.

Thackston, E. S. S., Casademont, T. M., Carter, L. M., Russell, P., Dypvik, H., Alwmark, S., et al. (2024). Observations of igneous subsurface stratigraphy during the jezero crater floor rapid traverse from the RIMFAX ground-penetrating radar. *The Planetary Science Journal*, *5*(8), 191. https://doi.org/10.3847/psj/ad6445

Tice, M. M., Hurowitz, J. A., Allwood, A. C., Jones, M. W., Orenstein, B. J., Davidoff, S., et al. (2022). Alteration history of Séítah formation rocks inferred by PIXL x-ray fluorescence, x-ray diffraction, and multispectral imaging on Mars. *Science Advances*, *8*(47), eabp9084. https://doi.org/10.1126/sciadv.abp9084

Tosca, N. J., Tice, M. M., Hurowitz, J. A., Pedersen, D. A. K., Henneke, J., Mandon, L., et al. (2025). In situ evidence for serpentinization within the Máaz formation, Jezero crater, Mars. *Science Advances*, *11*(27), eadr8793. https://doi.org/10.1126/sciadv.adr8793

Traxler, C., Ortner, T., Hesina, G., Barnes, R., Gupta, S., Paar, G., et al., (2022). The PRoViDE framework: Accurate 3D geological models for virtual exploration of the Martian surface from Rover and orbital imagery. 3D digital geological models: From terrestrial outcrops to planetary surfaces. https://doi.org/10.1002/9781119313922.ch3

Treiman, A. H., Hernández-Montenegro, J. D., Wiens, R. C., Wade, L., VanBommel, S., Van Beek, J., et al. (2025). The Brac/Dourbes olivine-cumulate rock, Séítah formation, Jezero crater floor, Mars: Its parent magma, and relation to basalts of the Máaz formation. *Journal of Geophysical Research: Planets*, *130*(4), e2024JE008539. https://doi.org/10.1029/2024je008539

Udry, A., Ostwald, A., Sautter, V., Cousin, A., Beyssac, O., Forni, O., et al. (2023). A Mars 2020 perseverance SuperCam perspective on the igneous nature of the Máaz formation at Jezero crater and link with Séítah, Mars. *Journal of Geophysical Research: Planets*, *128*(7), e2022JE007440. https://doi.org/10.1029/2022je007440

van Wyk de Vries, B., Márquez, A., Herrera, R., Bruña, J. G., Llanes, P., & Delcamp, A. (2014). Craters of elevation revisited: Forced folds, bulging and uplift of volcanoes. *Bulletin of Volcanology*, *76*(11), 1–20. https://doi.org/10.1007/s00445-014-0875-x

Werner, S. C. (2009). The global Martian volcanic evolutionary history. *Icarus*, *201*(1), 44–68. https://doi.org/10.1016/j.icarus.2008.12.019

Wiens, R. C., Udry, A., Beyssac, O., Quantin-Nataf, C., Mangold, N., Cousin, A., & SuperCam Team. (2022). Compositionally and density stratified igneous terrain in Jezero crater, Mars. *Science Advances*, *8*(34), eabo3399. https://doi.org/10.1126/sciadv.abo3399

Withjack, M. O., Olson, J., & Peterson, E. (1990). Experimental models of extensional forced folds. *AAPG Bulletin*, *74*(7), 1038–1054.

Wogsland, B. V., Minitti, M. E., Kah, L. C., Yingst, R. A., Abbey, W., Bhartia, R., et al. (2023). Science and science-enabling activities of the SHERLOC and WATSON imaging systems in Jezero Crater, Mars. *Earth and Space Science*, *10*(11), e2022EA002544. https://doi.org/10.1029/2022ea002544

Yonkee, W. A., & Weil, A. B. (2015). Tectonic evolution of the Sevier and Laramide belts within the North American Cordillera orogenic system. *Earth-Science Reviews*, *150*, 531–593. https://doi.org/10.1016/j.earscirev.2015.08.001